Reconstruction of past exposure to natural hazards driven by historical statistics: HANZE v2.0

Dominik Paprotny, Matthias Mengel

Potsdam Institute for Climate Impact Research (PIK), Member of the Leibniz Association,
P.O. Box 60 12 03, 14412 Potsdam, Germany

Correspondence to: Dominik Paprotny (dominik.paprotny@pik-potsdam.de)

Abstract. Understanding and quantifying the influence of climate change on past extreme weather impacts is vital for climate litigation, the loss and damage debate, and for building more accurate models to assess future impacts. However, the effects of climate change are obscured in the observed impact data series due to the rapid evolution of the social and economic circumstances in which the extreme events occurred. The model and data presented in this study (HANZE v2.0) aims at quantifying the evolution of key socioeconomic drivers in Europe since 1870, namely land use, population, economic activity and assets. It consists of algorithms to reallocate baseline (2011) land use and population for any given year based on a large collection of historical subnational- and national-level statistics, and then disaggregate data on production and tangible assets by economic sector into a high-resolution grid. Maps generated by the model enable reconstructing exposure within the footprint of any extreme event both at the time of the event and in any other moment in the past 150 years. This allows the separation of the effects of climate change from the effects of exposure change. In addition, HANZE v2.0 can be used for assessing socio-economic influences on hazard (e.g. effects of land use-change on hydrological extremes) and vulnerability (e.g. the changing structure of assets at risk).

1 Introduction

Global mean temperature has surpassed 1°C warming compared to pre-industrial times. There is growing research that quantifies the effects of the changing climate on the world's natural, managed and human systems. While evidence for natural systems tightly linked to the climate is mounting (Gudmundsson et al. 2021, Grant et al. 2021), less quantification is available for systems with strong additional drivers of change (O'Neill et al. 2022). Case studies have indicated strong influence of additional drivers especially for floods, where the uncertainty of the present risk is already high. For example, flood risk in the Rhine basin was found to be least sensitive to change in atmospheric forcing, but more to changes in reservoir capacity, dike height, land use, asset value or private precautionary measures (Metin et al. 2018). Vousdoukas et al. (2018) has shown that flood protection was the biggest source of uncertainty in coastal flood risk assessments in test sites in the Iberian Peninsula.

28 Estimates on the value of assets in a given location (exposure) and flood vulnerability functions, which indicate the share of

29 assets that are lost at a given intensity of flood, vary drastically between countries (Jongman et al. 2012, Huizinga et al. 2017,

30 Carisi et al. 2018, Paprotny et al. 2021). Windstorm damage in Europe was shown not to increase after correcting for exposure

31 increase (Barredo 2010) with attribution being complicated by contrasting trends in hazard (Dawkins et al. 2016) and very

32 high uncertainty on vulnerability functions (Welker et al. 2021). Finally, only a small fraction of wildfires in Europe are caused

33 by natural sources, making the human factors fundamental in understanding the frequency of those disasters (Ganteaume et al.

34 2013).

35 The IPCC AR6 (IPCC 2022) refines a framework introduced in IPCC AR5 to address the attribution of impacts in systems

36 with strong additional drivers. In such systems a stable baseline not changing in time is not plausible in the absence of climate

37 change. They suggest creating a time-evolving counterfactual impact baseline in which all historical forcings are equal to the

38 factual observations except for the counterfactual climate change signal. One can then attribute the changes due to historical

39 climate change through comparison of the simulated counterfactual impact baseline with the simulated factual impacts. A

40 precondition for such attribution exercise is that the impact models used for the simulations reflect the causal structure from

41 drivers to impacts, which is the task of model evaluation. A proposition of a counterfactual forcing to attribute impacts to

42 trends in historical climate has recently been introduced to the Inter-Sectoral Impact Model Intercomparison Project ISIMIP

43 (Mengel et al. 2021). High-quality simulations of factual past and counterfactual baseline necessitate high-quality data of the

44 additional drivers of historical impacts.

45 Many studies indicated no upwards trend in natural hazard direct economic loss in Europe, USA or Australia when corrected

46 for growth in exposure (Barredo 2009, Simmons et al. 2013, Paprotny et al. 2018b, McAneney et al. 2019, Pielke 2021).

47 However, in those cases increase in hazard caused by climate change could have been compensated by decline in vulnerability,

48 as was indicated for several parts of the world for floods by Sauer et al. (2021). Adaptation could further reduce impacts

49 (Kreibich et al. 2015, Steinhausen et al. 2022), both through prevention (e.g. higher flood defences) or reducing vulnerability

50 through collective (emergency response) and individual preparedness (flood- and fireproofing houses). Vulnerability is not

51 directly observable, therefore highly uncertain. To quantify it and reduce the uncertainty in climate impact attribution, high-

52 quality hazard, exposure and impact data are needed. The hazard component is being heavily researched (Dawkins et al. 2018,

53 Harrigan et al. 2020, Almar et al. 2021, IPCC 2021) and impact data are increasingly available at least for recent events (Stucki

54 et al. 2014, Antonescu et al. 2017, Papagiannaki et al. 2022). Quantifying changes in exposure, such as land use type,

55 population, economic output, value of assets, and the uncertainty of it is vital not only due to its large direct influence on the

56 observed impacts, but also indirect effects. In case of floods, high-exposure areas tend to be better protected (Scussolini et al.

57 2016) and less vulnerable (Formetta and Feyen 2019), while land-use can locally modulate river discharge stronger than

58 climate change (Sebastian et al. 2019).

59 Available historic reconstructions of exposure have limited utility for climate change attribution in a long perspective, either

60 due to low resolution, limited spatial coverage or covering only a particular component of exposure. For example, HILDA

61 (Fuchs et al. 2013, 2014, 2015) includes only highly aggregated land cover for the European Union countries, though with a

62 high 1 km resolution covering years 1900 to 2010. The global dataset HYDE (Klein Goldewijk et al. 2017) spans from years

63 10,000 BC to 2017 AD for both land-use and population, but has a resolution of only 5 arc-minutes (9 km on the equator).

64 HYDE is applied extensively in both global climate and climate impact modelling, including ISIMIP (Frieler et al. 2017).

65 Based on HYDE, a GDP disaggregation was also created for ISIMIP (Geiger 2018), which was used in the global flood

66 attribution study by Sauer et al. (2021). Analysing flood and wildfire risk in particular require very high resolution of exposure

67 data because they are highly local phenomena. Yet, high-resolution population data is available at best for a few timesteps per

68 dataset, going back no further than 1975 (Leyk et al. 2019). Disaggregation of economic data is mostly limited to a single

69 predictor of economic activity, such as population density (Kummu et al. 2018), or night-time lights (Eberenz et al. 2020).

70 HANZE v1.0 (Paprotny et al. 2018a) was the first exposure dataset with resolution matching pan-European flood hazard maps,

71 namely 100 m (Vousdoukas et al. 2016, Paprotny et al. 2017, 2019), covering the years 1870 to 2015 with a short-term

72 projection to 2020. It was designed specifically to enable the analysis of exposure and land-use change within flood footprints

73 of known historical floods (Paprotny et al. 2018b, Barendrecht et al. 2019, Zanardo et al. 2019). The model is concentrated on

74 the most densely populated and economically valuable areas: cities, industry, infrastructure and agriculture. Conceptually,

75 HANZE is similar to HYDE. They are in essence a downscaling of land-use and demographic trends from aggregated historical

76 statistics to a high-resolution grid. However, HYDE uses a coarser grid and extends to a much longer (12,000 years) timescale,

77 with an orientation on changes in land-use rather than economic value. In summary, HANZE aims at reliably modelling high-

78 exposure areas, while keeping the model's methods explicit and the computation fast.

79 We present the input data sources, processing steps and model for generating highly detailed exposure data for Europe from

80 1870 to present for HANZE v2.0 to facilitate the attribution of historical impacts. It builds on the original HANZE v1.0 release,

81 but many changes were made to the model (Table 1). Most crucially, its code was written anew in an open-source language

82 and is now made public together with all input data. For HANZE v1.0, only the results and selected inputs were released. The

83 general setting of the model (section 2.1) remains the same, though the spatial coverage and temporal resolution have been

84 improved, and an additional output map on soil sealing degree was added (Table 1). Many improvements to input data were

85 made, particularly administrative and demographic spatial layers (section 2.2) as well as historical statistical data (section 2.3).

86 They are accompanied by revised methods, especially on population distribution (section 2.4) and economic disaggregation

87 (section 2.5). More extensive validation was carried out than before (section 3.2) and a quantification of the uncertainty of

88 reconstructing past exposure was added to the model (section 3.2.4). We do not include flood impact data as in HANZE v1.0,

89 because we are working on an extensive revision to be described in an additional manuscript (see also section 4).

90

91 **Table 1. Comparison between releases of HANZE model and dataset.**

Aspect	HANZE v1.0 (Paprotny et al. 2018a)	HANZE v2.0 (this study)
Spatial coverage	37 countries and territories	42 countries and territories
Temporal coverage	1870–2020	1870–2020
Spatial resolution	100 m	100 m
Temporal resolution	10-yearly (1870–1970) 5-yearly (1970–2020)	10-yearly (1870–1950) 5-yearly (1950–2000) Annual (2000–2020)
Output exposure maps	Land cover/use, population, GDP, fixed assets	Land cover/use, population, GDP, fixed assets, soil sealing degree
Validation	Population change only	Population disaggregation, population & land use change
Uncertainty quantification	None	Included in parts of the modelling chain
Probabilistic outputs	Not possible	Can be computed (population, GDP, fixed assets per hazard zone)
Implementation language	MATLAB 2016a, Python 2.7	Python 3.9
Code availability	Not published	Openly available
Input data availability	Partial	All data published
Flood impact data	1564 events (1870–2016)	Not included (updated data will be added in the future)

92

93 This paper presents the model's methodology, validation and an overview of the results. The code of HANZE v2.0 are available

94 in an online repository (https://dx.doi.org/10.5281/zenodo.6826536) together with a documentation, which only describes the

95 methodology, though more extensively than this paper by adding many minor technical details and more detailed tables/figures

96 on input data. The input and output data are stored in separate repositories due to size (see "Code and data availability" at the

97 end of the paper).

98 **2 Methods**

99 **2.1 Overview**

100 HANZE v2.0 is a model for generating historical exposure data through operations on raster data. A summary of the model's

101 workflow is presented in Fig. 1. The starting point is a set of high-resolution rasters with data on population and land cover/use

102 for a specific benchmark year. Those "baseline" maps were created from 100-m resolution data (2.2.1), except population,

103 which was disaggregated from a 1-km resolution (2.2.2). The model modifies the baseline maps by redistributing land

104 cover/use and population until they match the total population and area of different land-use classes defined per subnational

105 administrative unit for each timestep. For each such unit, we collected aggregate socioeconomic statistics (section 2.3). Various

106 land-use types (urban, industrial, agriculture etc.) are modelled using different methods and several auxiliary static maps

107 described in section 2.4. Based on land-use changes, the soil sealing map is modified (section 2.4.13). Finally, the model

108   disaggregates statistical data on gross domestic product (GDP) and fixed asset stock into a 100-m grid, based on the distribution

109   of population and different land-use types (section 2.5). The model is applied using data covering 42 countries and territories

110   over the period 1870–2020 (see Supplementary Fig. S1).

111
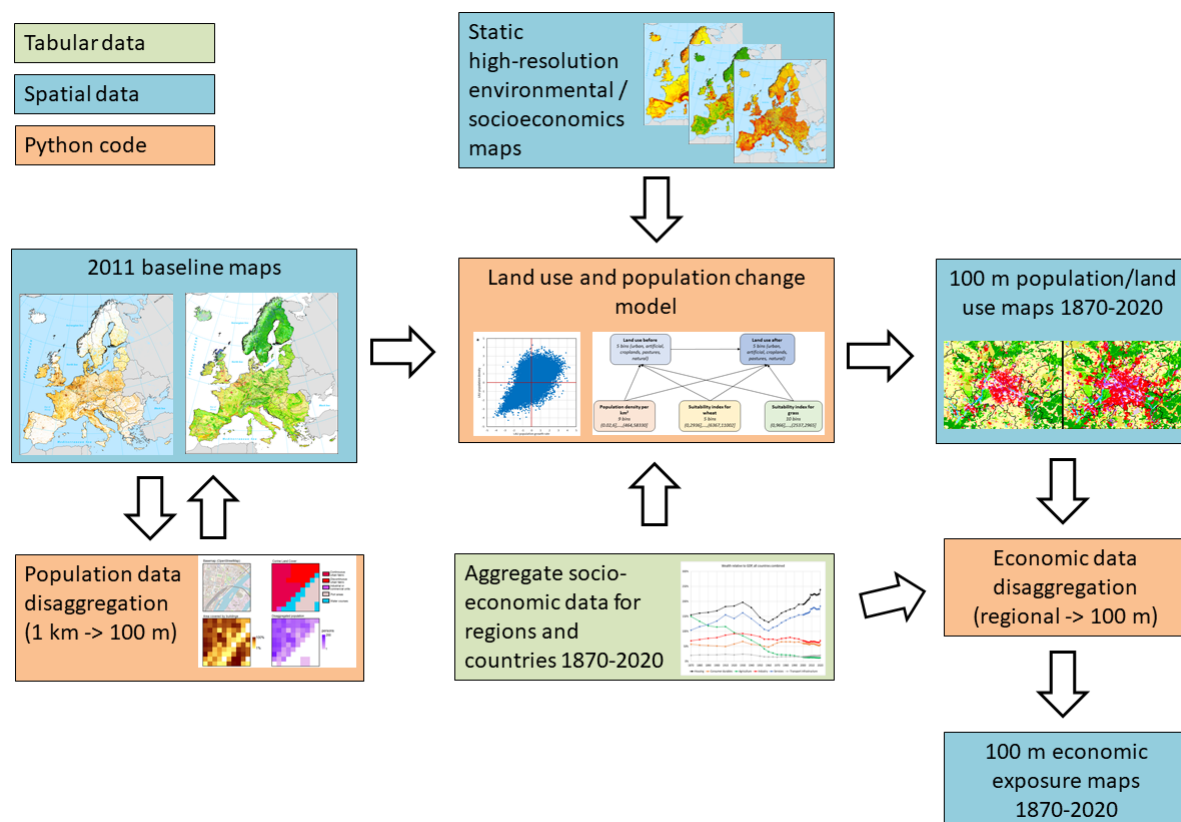
Figure 1. HANZE v2.0 workflow.

113

114

115   **2.2 Baseline maps**

116   Four baseline maps are a set of raster layers covering the study area, closely aligned in the temporal dimension, converted from

117   their native resolutions to a 100 m grid and adjusted to a single land mask based on Corine Land Cover (Table 2).

118

119 **Table 2. List of input historical socioeconomic data used by the model.**

Dataset type	Dataset name	Provider	Native resolution	Timestamp
Land cover/use	Corine Land Cover	Copernicus LMS	100 m	~2012
Soil sealing	Imperviousness Density	Copernicus LMS	20 m	~2012
Population	GEOSTAT	Eurostat	1 km	~2011
Administrative boundaries	NUTS regions	Own work	Vector map	~2010

120

2.2.1 Land cover/use, soil sealing degree

122 The baseline land cover/use is taken from Corine Land Cover (CLC) 2012, version 20u1, with open sea and some transitional
123 waters removed. The CLC 2012 map was created, in general, by manual classification of land cover patches from satellite
124 imagery collected during 2011–2012 (Copernicus Land Monitoring Service 2022). The inventory consists of 44 classes and
125 the minimum size of areal phenomena captured is 25 hectares. For quasi two-dimensional features (roads, railways, rivers
126 etc.), a minimum width of 100 m is used. The CLC dataset doesn't cover Andorra, hence a compilation of land use data from
127 other sources was carried over from HANZE v1.0 for Andorra (see section 2.1 in Paprotny et al. 2018a).

128 In many places natural land cover was replaced by artificial impervious surfaces. This impermeable cover has a significant
129 impact on hydrological properties of a given area and, consequently, on flood frequency and intensity. It is also an important
130 predictor of asset distribution. The baseline soil sealing map in our model is the Imperviousness Density 2012 dataset from
131 Copernicus Land Monitoring Service (2022). It was created by algorithmic classification of high-resolution satellite images
132 with a calibrated normalised difference vegetation index (NDVI). The native resolution of the dataset is 20 m, but we
133 aggregated it to 100 m for consistency with the land cover map.

2.2.2 Population

135 The baseline population map is based on the GEOSTAT population grid for the year 2011, version 2.0.1 (Eurostat 2022). This
136 dataset has a 1 km resolution and is based on the results of the 2011 round of European population censuses. 95% of the
137 population in the dataset is the actual enumerated and georeferenced during the census, with the remaining population
138 disaggregated from detailed subnational census returns by the European Commission Joint Research Centre. As in HANZE
139 v1.0, we disaggregate this dataset further to a 100 m grid. The disaggregation is done by combining methods "M1" and "M3"
140 described in Batista e Silva et al. (2013). "M1" denotes the 'limiting variable method' used in cartography for creating
141 dasymetric maps of population density. Briefly, it ranks land use classes according to density, then redistributes population
142 above a land use-specific threshold from less-dense to more-dense classes. The procedure is done the same way as in Paprotny

143 et al. (2018b), and only the population thresholds were updated due to the expansion of the study area and use of revised CLC
144 data. Additionally, the population disaggregation is now limited only to those CLC patches in which man-made structures
145 were present: either impervious surfaces from Imperviousness Density 2012 (see section 2.2.1) or buildings or streets from the
146 European Settlement Map (ESM) 2012 (Release 2017). All land-use classes in a 1 km cell were used if none of those auxiliary
147 datasets detected any artificial structures.

148 Method "M3" was applied afterwards, which distributes population within a land-use patch from method "M1" proportionally
149 to the degree of soil sealing. Buildings from ESM 2012 are used as a predictor, unless no buildings were indicated in a 1 km
150 cell, in which case Imperviousness Density 2012 was used instead. If no soil sealing was detected, roads and streets from ESM
151 2012 were used. This can happen mainly because ESM 2012 combined remote sensing data with multiple other sources, while
152 Imperviousness Density 2012 is entirely a remote-sensing based product. Hence, the population X_g in 100 m grid cell g is
153 equal to:

$$X_g = \frac{Z_g}{\sum Z_g} Y_{LG} S_{LG} \tag{1}$$

155 where Y_{LG} is the population density of land use patch L and 1-km grid cell G, S_{LG} is the area, and Z_g is the population of 100-
156 m grid cell g obtained from the power function divided by maximum population:

$$Z_g = \frac{B V_g^A}{8000} \tag{2}$$

158 where V_g is the imperviousness in grid cell g. The maximum population was defined as 8000 as all three datasets reached peak
159 population density around this value. The parameters A and B were derived empirically by fitting the power function to each
160 imperviousness variable (aggregated to 1 km) correlated with GEOSTAT population in the same grid cell.

161 The resulting population per 100 m grid cell was rounded to integers. Consequently, the population was added or subtracted
162 by iteratively reducing population numbers in 100 m cells starting with cells in which the smallest change in unrounded value
163 would change the rounded value. In some cases, more than one cell had equal values and the 1-km population couldn't be
164 matched. Then, population was added or subtracted by iteratively reducing population numbers by 1 at a time starting with
165 cells with the highest population. If again there were cases of multiple cells of equal values, cells with higher % of area covered
166 by structures were used. In extremely rare cases where no data was available or the % values were the same, the population is
167 added or subtracted randomly within the equal cells. The results of disaggregating the population for an example 1 km
168 GEOSTAT grid cell is presented in Fig. 2 (OpenStreetMap basemap is added to the figure for illustration only).
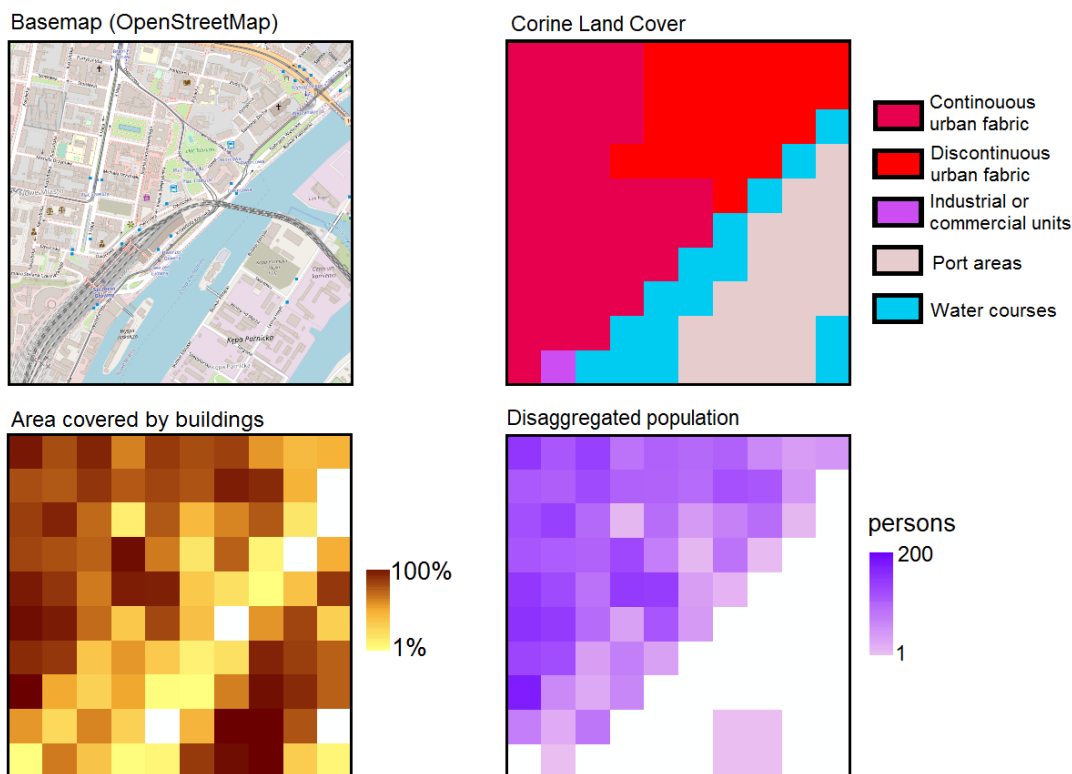
Figure 2. Disaggregation result and source data (population in the grid = 5230), contrasted with OpenStreetMap basemap for illustration. Fragment of the city centre of Szczecin, Poland (NUTS region PL424). Basemap © OpenStreetMap contributors 2022. Distributed under the Open Data Commons Open Database License (ODbL) v1.0. Corine Land Cover and area covered by buildings from Copernicus Land Monitoring Service (2022).

2.2.3 Administrative boundaries

The HANZE v2.0 model redistributes population, land cover/use and economic variables separately for each subnational administrative unit (hereafter, "regions"). Administrative boundaries change frequently within countries over time. Rather than changing the definitions of regions at each timestep of the model, we adjust historical statistical data to a single benchmark map. European Union's classification of subnational units, the Nomenclature of Territorial Units for Statistics (NUTS), version 2010, is used in HANZE v2.0. The most detailed level of the classification, NUTS level 3 is applied. For this study we prepared a new, high-resolution map of NUTS regions due to the low precision and non-permissive licence of the semi-official NUTS map available through Eurostat (Eurostat 2022). We compiled the new map using openly-available data from national geospatial agencies and OpenStreetMap, manually corrected where necessary. A detailed list of source data is provided in Supplementary Table S1. The map was adjusted to only cover land areas, in alignment to the baseline CLC map (section 2.2.1) and converted into a 100 m grid. As Kosovo and Bosnia and Herzegovina are not currently covered by NUTS, we artificially

185 coded their administrative divisions in a manner consistent with the NUTS system. Our study's domain contains 1422 regions
186 in total. As noted, the input historical statistics that drive the model were recomputed where necessary to match our high-
187 resolution map of NUTS regions (see section 2.3).

2.3 Input socioeconomic data

189 The input database of historical socioeconomic statistical data was created by revising the data from HANZE v1.0. It contains
190 data on the main socioeconomic drivers of exposure at regional level. The variables of the database are listed in Table 3.
191 Further it contains fixed asset stock relative to GDP in six sectors, defined at country level. The database was compiled from
192 375 different sources (compared with 271 in HANZE v1.0): websites and publications of national statistical institutes and
193 international agencies, working papers of national banks and economic research institutes, and academic research papers,
194 dating from 1872 to present. Detailed information on the source of every single data point in the database, and transformations
195 made to adjust data to NUTS version 2010 are described within the datasets provided in the HANZE data repository
196 ("Region_database_population_lu.xlsx" and "Region_database_economy.xlsx"). The data was compiled every decade from
197 1870 to 1950, every 5 years until 2000 and annually until 2020. Detailed definitions of database variables are presented in the
198 online documentation provided in the code repository (see "Code and data availability").
199

Table 3. List of input historical socioeconomic data used by the model.

Variable	Unit	Resolution
Population	Thousands of persons	NUTS 3
Urban fraction	Urban population as % of total population	
Persons per household	Mean number of persons	
Croplands	% of total area	
Pastures		
Forests		
Infrastructure	Area covered by road/railway sites in ha	
GDP	Million euro in constant 2020 prices	
GDP from agriculture	% of total GDP	
GDP from industry		
Fixed assets in housing		Country
Fixed assets in agriculture	% of GDP from agriculture	
Fixed assets in industry	% of GDP from industry	
Fixed assets in services	% of GDP from services	
Fixed assets in infrastructure	% of total GDP	
Fixed assets in consumer durables		

Compared to HANZE v1.0, the main changes are: improvement in the quality of data through inclusion of more data sources (see Supplementary Fig. S2); addition of new countries (Albania, Bosnia and Herzegovina, Kosovo, Montenegro, North Macedonia and Serbia); addition of consumer durables (goods used by households for several years) as a category of fixed assets through integration of data and methods from Paprotny et al. (2020, 2022); addition of forest land cover data for the whole study area. In HANZE v1.0 forest data were only partially collected and were not used by the model. In this version v2.0 we use the forest data for 1870–2020 and include them in the modelling chain (section 2.4.12). Finally, though this update doesn't yet include flood impact data, the statistics needed for converting historical economic losses from nominal values (currency conversion factors and annual GDP deflators) were retained and updated with latest data sources.

2.4 Population and land-use model

The general approach, as noted in the introduction, is to modify the baseline population and land cover/use map for every timestep. This is done sequentially for different CLC classes, so that a class that is modified in a given step doesn't alter those that were modelled beforehand. The order of the modelling steps is as follows:

1.   Special cases (section 2.4.1)
2.   Sub-regional population redistribution (2.4.2);
3.   Urban fabric and urban population redistribution (2.4.3);
4.   Airports (2.4.4);
5.   Reservoirs (2.4.4);
6.   Rural population redistribution (2.4.5);
7.   Industrial or commercial units (2.4.6);
8.   Road/railway sites (2.4.7);
9.   Construction sites (2.4.8);
10. Other artificial land (2.4.9);
11. Croplands (2.4.10);
12. Pastures (2.4.10);
13. Burnt areas (2.4.11);
14. Natural areas (2.4.12);
15. Soil sealing degree map adjustment (2.4.13);

A summary of the modelling approach, and the rationale is explained, per land cover/use class from the CLC dataset, in Table 4. It also highlights how important is each CLC class to the exposure analysis, in terms of population and estimated fixed asset value. Detailed information is provided in the following subsections, as referenced in the numbered list above.

Table 4. Summary of observed historical changes, the modelling approach used in this study, and the relevance of each land cover/use class in context of exposure to natural hazards. "% share" refers to the study area. Share of population (pop.) computed using disaggregated population (section 2.2.2) and share of fixed assets (f. a.) estimated using disaggregated economic data (section 2.5). Each land cover/use class includes reference to the appropriate section of the text.

Land cover/use	CLC codes	% share (2011)			Observed changes	Approach
		area	pop.	f. a.		
Urban fabric (section 2.4.2–3)	111, 112	3.3	87.6	72.0	Population density decrease in urban core and rural areas, rapid growth in suburban zones observed in municipal-level population data. Growing share in urban population overall and rapid increase in housing demand due to decline in average population per household	Sub-regional population redistributed based on baseline population density (with uncertainty estimation), urban population changed according to distance for city 'cores', urban fabric added/removed when large increases/decreases of urban population occur. Total & urban population defined at NUTS3 level in historical statistics
Industrial or commercial units (2.4.6)	121	0.6	0.7	19.2	This class expanded 16% between 2000 and 2018, representing addition of physical capital that contributed to GDP growth	Land use added/removed based on centroid distance according to NUTS3 industrial/services growth, with elasticity of spatial growth calibrated for 2000–2018
Road/railway sites (2.4.7)	122	0.1	0.0	0.3	Length of railways and motorways increased four-fold since 1870, spreading from large cities; construction sites most frequently transitioned to this class between CLC datasets.	Grid cells located furthest from the urban centres are removed first when going back in time until the total area per region matches the value in the NUTS3 database; after 2011, construction sites are prioritised for new road/railway sites
Airports (2.4.4)	124	0.1	0.0	0.2	1589 airports in CLC 2012 were all built since 1908; 9 new airports present in CLC 2018	Airports are added/removed from map based on year of construction
Construction sites (2.4.8)	133	0.0	0.0	0.1	Most construction sites transition to another land use during the 6-year periods between CLC datasets.	Construction sites replaced by natural/agricultural land for 1870–2004 and allowed to transition to other artificial surfaces after 2011.
Urban green spaces (2.4.9)	141, 142	0.3	0.1	0.7	Two-thirds of green urban areas, sport and leisure facilities border either urban fabric, industrial sites, road/railway sites, or airports in the CLC 2012 inventory	Urban green spaces which bordered CLC 111–122 and 124 patches in the baseline map are removed if in a given timestep they were not adjacent anymore
Other artificial (2.4.9)	123, 132, 133	0.2	0.0	0.5	Many ports, mines, and dumps were constructed in the study area since 1870	Available data is too poor to collect the year of construction. Kept constant and are not allowed to interact with other land use classes*
Croplands (2.4.10)	211–223, 241–244	33.6	8.3	5.0	Transition probability from/to cropland in CLC inventory is	A Bayesian Network-based model is used for land-use transitions. Cells with the highest probability

					correlated with suitability to agriculture and population density.	of transition are added/removed until the total cropland area matches the value in the NUTS3 database
Pasture (2.4.10)	231	8.2	2.2	1.4	As above, but for pastures	As above, but for pastures
Forests (2.4.12)	311–313	31.6	0.7	0.5	Expansion of agriculture and urban areas is partially to the expense of forest land (one-third of natural land lost in the CLC inventories)	Grid cells left unoccupied by modelling other land-use types are allocated to forest rather than other natural land if historical forest statistics indicate enough additional forested area
Other vegetated natural (2.4.12)	321–324, 411–422	14.9	0.2	0.1	Those areas have negligible exposure and are not of interest for the model	Kept constant, but can transition to/from agriculture
Burnt areas (2.4.11)	334	0.0	0.0	0.0	Almost none of burnt areas in CLC 2012 was present in CLC 2006 or 2018	As burnt areas are transitory, areas present in the baseline map are removed for 1870–2006 and 2018–2020.
Water bodies (2.4.1, 2.4.4)	512	2.3	0.0	0.0	1118 large reservoirs in CLC 2012 were all built since 1882; 3 new reservoirs present in CLC 2018; Zuiderzee was much reduced by land reclamation between 1924 and 1975	Reservoirs and Zuiderzee polders are added/removed from map based on year of construction, enabling/disabling those areas for habitation and asset construction
Other natural (2.4.12)	331–333, 335, 423–511, 521–523	4.9	0.0	0.0	Those areas have negligible exposure and are not of interest for the model	Kept constant and are not allowed to interact with other land use classes, except cases described in 2.4.1 and 2.4.4

237

2.4.1 Special case

239 The model includes one special case, due to its influence on exposure distribution in the Netherlands. The *Zuiderzeewerken*
240 was a large-scale land-reclamation and flood-protection project, which resulted in the construction of large dikes and polders
241 in the Zuiderzee between the 1920s and 1970s (Supplementary Fig. S3). Zuiderzee was closed in 1932 by a large dike, turned
242 into a lake and further split in 1975 into IJsselmeer and Markermeer. Cities, infrastructure and farmland were created on the
243 reclaimed land, mainly in the province of Flevoland. It has a population of more than 400,000 today, but before 1942 it
244 consisted only of the small island town of Urk and the uninhabited island of Schokland (the province was formally established
245 in 1986). Therefore, all artificially-created land is removed from the land cover/use map and turned into inland water (CLC
246 512) for years before the year of completion of individual polders. The population is also removed and not considered in the
247 population and land-use redistribution for those years, hence this modelling step is done before all others.

2.4.2 Sub-regional population redistribution

249 Substantial redistribution of population within European countries occurred in modern times. Here, we model sub-regional
250 (i.e. below NUTS3 level) population change for 1870–2020 based on empirical observations from a dataset of population

change between 1961 and 2011 at the level of local administrative units (LAUs). We created the dataset for this study mostly through merging tabular and spatial data produced in various years that is available through Eurostat (2022). Details on how the data were created and their visualisation is provided in Supplementary Text S1. Population trends for around 109,000 LAUs indicate:

- Declining population in urban cores that are the most centrally located and densely populated parts of cities
- Rapid growth of suburban zones around urban cores
- Declining population of rural areas

The first two changes are largely driven by the change in number of persons per household. Even when the population of a city is stagnant, smaller families in each dwelling result in an increased demand for housing. Those extra dwellings had to be constructed mostly outside the urban cores, where the supply of housing is largely fixed. Clark (1951) has shown that this trend has been present in major European cities since the early 19th century, flattening the population density curve in relation to the distance from the city centres. At the same time, migration from rural to urban areas has reduced population in rural areas and exacerbated the growth of suburbs.

Here, we model the rate of change of population within each NUTS3 region, where total population is defined by historical statistics, using the empirical relationship between population density and historical rates of change. To capture the uncertainty of the correlation, two univariate copulas that correlate population density from LAU data with population growth are applied (Fig. 3):

- the Gaussian copula using data from LAUs with population density below 1500 persons per km^2 that correlates population density from LAU data with population growth (Spearman's r = 0.69) and
- the Frank copula using data from LAUs with a population density above 1500 persons per km^2 that correlates "agglomeration density" with population growth (Spearman's r = -0.36).
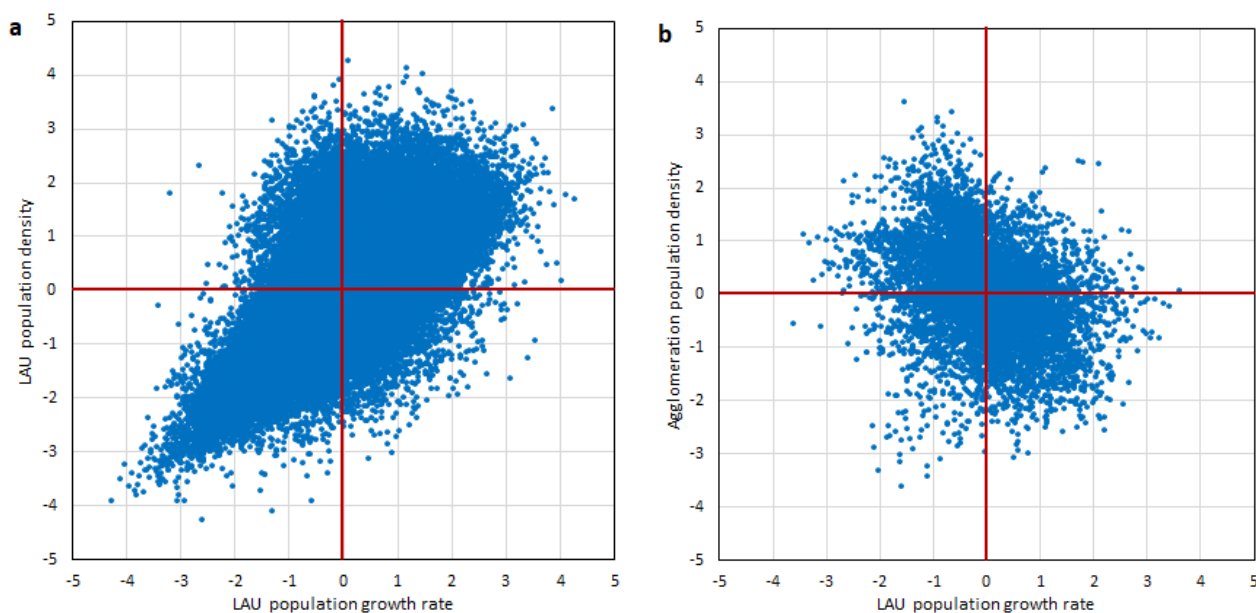
Figure 3. Empirical copulas of the dependency between population growth (1961–2011) relative to national growth, and population density (2011) in two different forms (a – local density, b – agglomeration density). Left copula (a) is applicable to population densities below and right (b) above 1500 persons per km².

The "agglomeration density" per LAU is the average of the kernel density computed with the 1 km GEOSTAT population grid and a 10-km radius. Therefore, it indicates the size of agglomeration that a high-density LAU is part of. This "agglomeration density" is a better predictor of population change than population density of individual LAUs. Only LAUs from NUTS3 regions with at least 10 LAUs were included to quantify the copulas to avoid using large, heterogenous LAUs. The copulas were chosen based on a goodness-of-fit test (Genest et al. 2009). The threshold of 1500 persons per km² for copula selection gave the best results in validation. Coincidentally, but unsurprisingly, it is also the threshold used to define high-density population clusters by Eurostat (2022), and in turn to classify LAUs as urban.

The LAUs from the Eurostat dataset applied here do not have complete coverage, have lower geometric accuracy than our NUTS3 map, and the size of LAUs varies substantially between countries. Therefore, a set of "virtual" LAUs (hereafter, "VLAUs") was constructed. Every VLAU consists of an urban patch from Corine Land Cover 2012 and its nearest neighbourhood (Supplementary Fig. S5). Disaggregated population in 100 m resolution was then assigned to each VLAU to compute population density. For each timestep in the model, the copulas are sampled 10,000 times to obtain an estimate of annual population growth (geometric average of 50-year growth rate). The population of a VLAU in year t and 2011 is then:

$$P_{t,VLAU} = P_{2011,VLAU}(1 + A)^{2011-t} \qquad (3)$$

289

290 where A is the annual growth rate (in %) from the copula model. To avoid unrealistic changes, mainly for areas with very low

291 population density, population growth is capped: $-2.257\% < A < 1.6464\%$, which corresponds to a 10-fold decline or 25-

292 fold increase between 1870 and 2011. The analysis is done separately for each NUTS region, covering VLAUs or their parts

293 located within a given region. After the population of all VLAUs was computed for a given NUTS region, the difference

294 between the combined population of VLAUs and the population of the NUTS region in a given year as defined in the historical

295 statistics is corrected by the same factor (relative to population) for every VLAU. The computation is done separately for urban

296 and rural areas, i.e. those covered by urban fabric and all others, respectively. The share of urban population in each NUTS3

297 region is determined by the historical statistics.

2.4.3 Urban/rural population and urban fabric

299 The population redistributed at sub-regional level is further adjusted spatially, separately for urban and rural areas. As noted

300 in section 2.4.2, assuming fixed supply of housing in already built-up areas, the population change in urban areas and expansion

301 of those areas (i.e. urban fabric, or CLC classes 111 and 112) is driven by change in the total number of urban households. As

302 the population has grown but the average number of persons per household has declined throughout Europe since the 19th

303 century, the demand for housing increased substantially. The movement of population to the edges of cities (suburbanization)

304 is accompanied by the reduction of population density in the urban "cores" where a similar number of households contains a

305 declining population stock. This process of flattening population distribution as a logarithmic function of distance from urban

306 cores was quantified by Clark (1951) and many subsequent studies. By taking the total urban population U and average number

307 of persons per household H (household size) from our historical statistics (section 2.3) we can compute the total number of

308 urban households $N_t = H_t/U_t$ in year t for every region. We simulate how the increase in N_t has caused urban fabric to expand

309 through construction of new housing and related infrastructure in previously undeveloped areas. In rare cases, within recent

310 years, there has been a decline in urban households over time. This so far has led to dwellings becoming vacant rather than a

311 contraction of the area of the urban fabric.

312 The modelling operates by modifying, for a given timestep t, the population per urban fabric grid cell P_{2011} defined in the

313 baseline population map. This is done separately and independently for each VLAU, where the total baseline urban population

314 is $U_{2011} = \sum P_{2011}$. The aim of this modelling step is to generate a new population map, where $\sum P_{2011}$ matches U_t, which in

315 turn is the total urban population of a VLAU in timestep t. U_t is defined beforehand for each VLAU, as it is a proportional

316 adjustment to the total population of all VLAUs in a given NUTS3 region, calculated already in section 2.4.2, to the total urban

317 population of a NUTS3 region defined in the historical statistics. We therefore know the expected urban population in a VLAU

318 and have to modify the population map to reproduce the historical changes in the size of the urban population and change of

319 their distribution within the cities. Changes in household size are taken from historical statistics at NUTS3 level. The procedure

320 is done stepwise:

321   1. In every urban fabric grid cell in a VLAU, the grid-cell population P in year t is modified relative to the 2011 baseline

322   to account for change in household size:

$$P_t = P_{2011} \frac{H_t}{H_{2011}} \tag{4}$$

324 where H is the average household size, determined for each NUTS3 region;

325   2. All grid cells in a region are ranked by distance from urban centres (explained further in the text), where the highest-

326   ranked cells are the closest to any urban centre.

327   3. Surplus population S_t is calculated:

$$S_t = U_{2011} \frac{H_t}{H_{2011}} - U_t \tag{5}$$

329 where $U_t = \sum P_t$ is the total urban population in the VLAU. The modelling ends here if $S_t = 0$, but that is almost never the

330 case. S_t is usually positive or negative, and indicates how many persons, after adjusting the population map to the household

331 size of historical level H_t, have to be removed or added to the map in order to match the historical total population U_t.

332 Depending on whether a year before or after the baseline is modelled, four combinations of S_t and t could be discerned, as

333 indicated in Table 5.

334

Table 5. Possible combinations of surplus population St and timestep t, contrasted with illustrative examples taken from the database of historical statistics (section 2.3). These examples use data at NUTS3 level, but the calculation itself is done on the more detailed level of VLAUs.

Case	Example (region, NUTS3 code and historical data)	Approach
A $S_t > 0$, $t < 2011$	Potsdam, Germany (DE404) U_2011=152,656, H_2011=1.80, N_2011=84,668 U_1960=114,202, H_1960=2.96, N_1960=38,569 S_1960=136,500	The city more than doubled the number of households since 1960, which had to be accommodated through expanding the urban area with new housing districts. Hence, part of urban fabric in 2011 was created between 1960 and 2011 and has to be removed from the modelled exposure map for 1960.
B $S_t < 0$, $t > 2011$	Szczecin, Poland (PL424) U_2011=398,652, H_2011=2.40, N_2011=166,313 U_2020=389,660, H_2020=2.08, N_2020=187,247 S_2020=-43,563	The city has increased the number of households since 2011, despite population decline. Hence, areas available for build-up in 2011 are converted into urban fabric in the 2020 map to the extent needed to accommodate the new households.
C $S_t > 0$, $t > 2011$	Vidzeme region, Latvia (LV008) U_2011=127,541, H_2011=2.53, N_2011=50,391 U_2020=111,053, H_2020=2.45, N_2020=45,309 S_2020=12456	Number of urban households in the region declined since 2011, which resulted in some dwellings being vacated. The urban fabric therefore doesn't change in the 2020 map, but the population is reduced in urban areas throughout the region.
D $S_t < 0$, $t < 2011$	Liverpool, United Kingdom (UKD72) U_2011=466,415, H_2011=2.80, N_2011=203,701 U_1970=606,979, H_1970=2.26, N_1970=216,856 S_1970=-36,819	Number of urban households in the city declined between 1970 and 2011, which resulted in some dwellings being vacated. The urban fabric therefore doesn't change in the 1970 map, but the population is higher in urban areas of the city in 1970.

In the two cases A and B, i.e. $S_t > 0, t < 2011$ and $S_t < 0, t > 2011$, the number of households, and therefore extent of urban areas, expanded over time. For timesteps before 2011 this means that some of the urban fabric has to be removed from the baseline map (case A), while for timesteps after 2011 more urban fabric has to be added (case B). The changes in grid-cell population P will depend on the distance from urban centres d. The distance from urban centres used here is a weighted average of different measures of population centres ("combined distance") in order to capture the multiple levels of hierarchy existing in urban networks. Five different datasets were tested and, based on a calibration process explained in the Supplementary Text S2, four of those datasets were selected for the combined distance from urban centres. The datasets and their weights are as follows:

- Arbitrary centres of large agglomerations (more than 300,000 persons in 2018) and capital cities (United Nations 2018), with a weight of 1.0;
- Centroids of high-density population clusters (Eurostat 2022), with a weight of 1.5;
- Centroids of cities included in the Urban Atlas 2018 (Eurostat 2022), with a weight of 2.0;

- Centroids of Corine Land Cover 2012 urban patches, with a weight of 0.5.

The fifth dataset, not included in the combined distance, were population clusters from Eurostat (2022). The combined distance is computed per each grid cell. Then, the modelling continues depending on the case:

- Case A: urban grid cells are iteratively removed going backwards from the base year 2011 starting with the lowest-ranked ($i = 1$), and their population is reduced by proportion D:

$$P_{t,i} = P_{t,0}D \tag{6}$$

Proportion D is based on the logarithm of distance from urban centres d in hectometres:

$$D = \left(1 - \frac{\ln(d)}{\ln\left(\arg\max\{d\}\right)}\right) \tag{7}$$

At each iteration the surplus is reduced by the amount of population redistributed:

$$S_{t,i} = S_{t,i-1} - P_{t,0}(1 - D) \tag{8}$$

The calculation continues until $S_{t,i} = 0$. However, if at any iteration there is more population in grid cell(s) than remaining surplus, i.e.:

$$\sum P_{t,0}(1 - D) = S_{t,i-1} \tag{9}$$

the population is reduced by the available amount, split proportionally to grid cell population if there are more cells with the same rank:

$$P_{t,i} = P_{t,0}\left(1 - \frac{S_{t,i-1}}{\sum P_{t,0}}\right) \tag{10}$$

- Case B: cells where urban expansion most likely took place are identified using the land-use transition model described in section 2.4.8, starting with cells with the highest probability of transition. If more cells were given the same likelihood of transition to urban fabric than necessary to assign the additional population, the cells within that group were ranked according to distance from the urban centre. The population in the highest-ranked cells, i.e. iteration $i = 1$, is set to the maximum population per grid cell in the VLAU, reduced by proportion D from eq. 7:

$$P_{t,i} = \arg\max\{P_{t,0}\}D \tag{11}$$

At each iteration the surplus is increased by the amount of population redistributed:

$$S_{t,i} = S_{t,i-1} + P_{t,i} - P_{t,0} \tag{12}$$

The calculation continues until $S_{t,i} = 0$. However, if at any iteration there is more population to be redistributed than the available surplus, i.e.:

$$\sum P_{t,i} - P_{t,0} > -S_{t,i-1} \tag{13}$$

the surplus is distributed equally between all cells that were modified until this iteration (denoted n):

$$P'_{t,i} = P_{t,i}\left(1 - \frac{S_{t,n-1}}{\sum P_{t,i}}\right), i = \{1, \dots, n\} \tag{14}$$

If there are no available empty grid cells in the VLAU, the population of all urban grid cells is increased proportionally in the same way as in eq. 14.

- Case C and D: in those cases, the number of households declined over time, as some dwellings became vacant. The urban area remained unchanged, as urban fabric is not removed bar from very extreme cases. Before 2011, the population in all urban grid cells was added to the map (case C), while after 2011, removed (case D). The population was increased/decreased proportionally to the population in a given grid cell in 2011 (as in eq. 14).

Modelling the redistribution of population in urban areas is intertwined with change in urban fabric area. In cases A and B, the urban area changes as a result of the growth in urban household number, in contrast to cases C and D, where the urban fabric is kept unchanged. As urban fabric is closely related with high population density, urban fabric grid cells are only removed from (case A) or added to (case B) the baseline map if the changes to population density is large enough. Consequently, urban fabric is removed in timesteps before baseline year 2011 only if the population in a grid cell was reduced to less than 9 persons. For timesteps after 2011, only an increase of population to more than 81 per 100 m grid cell resulted in transition to an urban fabric class. Both thresholds were obtained by calibrating the model to match the magnitude of change observed in the CLC inventories (2000–2018). Between 2000 and 2012, urban fabric expanded by almost 1.88 million ha, while between 2012 and 2018 only by 98,676 ha, according to the CLC data. By setting the population thresholds through calibration, the model correctly represents the effect of urban population change on land-use type. As shown in the results (section 3.2.3), the calibration was effectively applicable back to the year 1900.

2.4.4 Airports and reservoirs

Airports and reservoirs are large elements of infrastructure that first appeared within this study's timeframe. As the period of construction of those is usually well known and their number relatively small, they are removed or added to the baseline map based on the year of construction. We identified 1598 airports and 1121 large reservoirs in the study area by combining CLC maps (CLC classes 124 and 512) with global databases of those objects (Global Dam Watch 2021, OurAirports 2021). Though HANZE v1.0 also included such data, due to the addition of new countries, the use of a revised CLC map and updates to the global airport and reservoir databases, we recompiled the data on airports and reservoirs from scratch. An airport or reservoirs removed from the baseline map enables other land-use types to fill the empty space. An addition of such an object (after 2011) removes any population that was present there in 2011.

2.4.5 Rural population redistribution

Rural population is recalculated separately for each VLAU, by adjusting the grid cell baseline population proportionally to its value, so that it equals the expected population in that area. For years before the baseline, areas from which urban fabric was

409 removed are still considered urban for the purpose of this calculation. For years after the baseline, rural population in areas
410 that transitioned to urban fabric is no longer considered rural, hence the adjustment is made only to remaining rural cells in the
411 VLAU.

2.4.6 Industrial and commercial sites

413 The area covered by large industrial/commercial facilities was assumed to change proportionately to GDP generated in a
414 NUTS3 region by industry and services, in constant prices. Industrial grid cells (CLC class 121) located furthest from the
415 centroids of industrial land use patches are removed first when going back in time. For timesteps after the baseline year,
416 industrial grid cells closest to the centroids are added first. Industrial land use is only allowed to spread into uninhabited cells
417 of some CLC classes: construction sites (133), agricultural (211–244) and certain natural areas (311–324 and 333). However,
418 growth in GDP from industry and services is only partially driven by expansion of facilities, as the productivity of capital and
419 labour tends to increase. Indeed, CLC 121 class has grown between 2000 and 2018 (based on CLC 2012 and CLC-Changes)
420 by 16% in the study area, but GDP from industry and services increased by 32%. Therefore, the change in GDP from
421 industry/services is scaled by an elasticity of 0.45, so that modelled changes between 2000–2018 in the study area have the
422 same magnitude as observed in the CLC inventory. The industrial area A in region r and year t is as follows:

$$A_{r,t} = A_{r,2011}\left(\frac{G_{r,t}}{G_{r,2011}}\right)^{\varepsilon} \tag{15}$$

424 where ε is the elasticity and G_r is the regional GDP from industry/services according to the historical statistics at NUTS3 level.

2.4.7 Road and railway sites

426 The area covered by roads and railways before 2000 was assumed to change proportionately to the length of motorways and
427 railways. Historical data on the length of this type of infrastructure was included in the input database (Table 2). As
428 infrastructure was built firstly in large urban and industrial zones, infrastructure grid cells (CLC class 122) located furthest
429 from the urban centres are removed first when going back in time until the total area per region matches the value in the
430 database. Conversely, grid cells closest to the urban centres are filled with infrastructure for timesteps after the baseline year.
431 Infrastructure is allowed to spread only to particular CLC classes: construction sites (133), agricultural (211–244) and certain
432 natural (311–324 and 333). However, construction sites were prioritised over other CLC classes; all 'construction' grid cells
433 have to be used up before other CLC classes can be considered. The reason is that, apart from urban fabric or industrial sites
434 already considered in previous steps, road and railway sites are the most frequent outcomes of construction activity. We found
435 this pattern in the transitions of land-use in subsequent CLC inventories (2000–2018).

2.4.8 Construction sites

Construction sites (CLC class 131) are by definition a temporary land use, typically for only a few years. The CLC inventory shows that 76–81% of construction sites transition to another land use during the 6-year periods between CLC datasets (2000–2006, 2006–2012, 2012–2018). Therefore, for years 2005–2011, their area was assumed constant, while for years 1870–2004 all construction sites were removed from the dataset. After 2011, construction sites were allowed to transition into urban fabric, industrial sites, roads, railways, and airports (CLC 111–122 and 124), which was applied in the previous modelling steps, but otherwise kept unchanged.

2.4.9 Other artificial land

Green urban areas, sport and leisure facilities (CLC classes 141 and 142) are closely related to other artificial surfaces. Almost two-thirds of those CLC patches border either urban fabric, industrial sites, road/railway sites, or airports in the CLC 2012 inventory. Therefore, those patches of CLC classes 141 and 142 which bordered CLC classes 111–122 and 124 in the baseline map are removed if in a given timestep, if they do not border CLC classes 111–122 and 124 anymore due to application of previous modelling steps. Ports, mineral extraction, and dump sites (CLC classes 123, 131 and 132) are large elements of infrastructure like airports and reservoirs, but they are too numerous (almost 15,000 objects) and their history less traceable to apply the same approach as for airports. Therefore, their area is kept constant at every time step and they did not interact with other land use classes. Patches of this land use are removed from the map only in connection to reservoir or polder construction (see sections 2.4.1 and 2.4.4).

2.4.10 Agricultural areas

Evolution in agricultural areas and increase in urban fabric after the baseline year are computed primarily using a Bayesian Network (BN) model. The BN is trained with the CLC-Changes dataset, which records 1.2 million transitions involving patches of land larger than 5 ha, and CLC 2012 identifying land-use types that didn't transition between 2000 and 2018. The CLC-Changes and CLC 2012 inventory were sampled to obtain 513,915 cases of transition and an equal number of land-use patches being stable between 2000 and 2018. For each location, information from different raster datasets (on terrain, agricultural suitability, population density and urbanisation) were extracted as predictors of land-use changes. The sampling procedure and a list of all tested predictors is described in the Supplementary Text S3. The general concept is the same as in HYDE (Klein Goldewijk et al. 2011), i.e. that local suitability for agriculture determines where this land-use class expands (most-suitable of available land first) and contracts (least-suitable falls into disuse first).

As the land use information is categorical, a discrete BN was used. Land-use classes were collected into 5 bins (urban fabric, other artificial, croplands, pastures, natural). The bin with natural land excludes non-utilizable land cover types (CLC 331–332, 334–335, 421-523), which are not allowed to interact with either artificial or agricultural land use. The BN model was constructed iteratively, starting with a simple three-node network, where the "old" land-use class is the parent of the "new"

467 land-use class, and a single predictor variable is the parent of both land-use nodes. More complex BNs with more predictors
468 were respectively validated against a disjunct subset of samples of transitions and non-transitions not used for training (see
469 Supplementary Text S3). Iteratively, the best predictors, number of predictors and numbers of bins (into which continuous
470 variables were discretized) were selected. Three predictors were chosen, all of which are parents of the two land-use nodes
471 (Fig. 4):

- 472 Population density per VLAU – 9 bins;
- 473 Suitability index for wheat: output density (potential production divided by total grid cell area) for wheat under rainfed
- 474 conditions and high input level – 5 bins;
- 475 Suitability index for grass: agro-climatic potential yield for grass with an available water content of 200 mm/m (under
- 476 irrigation conditions) and high input level – 10 bins.

477 The two agricultural suitability indices were calculated by FAO (2022) in the Global Agro-Ecological Zoning version 4
478 (GAEZ) database, based on 1971–2000 climate. As the BN is quantified with a conditional probability table (CPT), this
479 configuration results in the CPT having 11,250 cells. Therefore, no more variables were added to avoid too few data points
480 quantifying cells of the CPT.

481
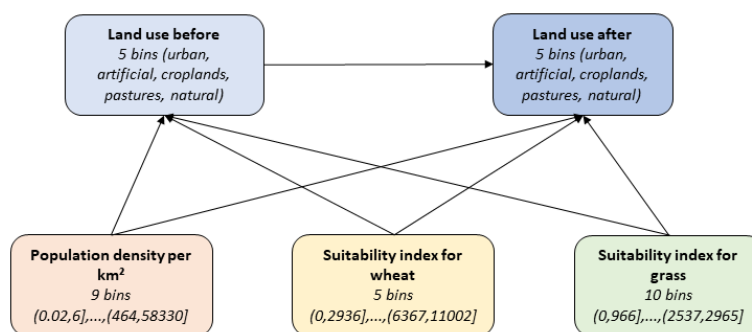
482
483 **Figure 4. Bayesian Network for land-use transitions with 5 nodes and 7 arcs. The nodes indicate the number of bins of the discrete**
484 **distributions and the intervals of the bins.**

485

486 Fig. 5 shows an example of application of the Bayesian Network. In this case, we know the present-day land use (croplands)
487 and that in some earlier timestep the total area of croplands in a NUTS3 region was lower than at present. Therefore, we want
488 to know the probability that land-use was different from croplands across the grid cells located in the region. Fig. 5a shows an
489 area that was most likely a cropland before as well, due to relatively high population density and good suitability for agriculture.
490 The area in Fig. 5b has lower suitability, which indicates a much higher probability that the area was used for other purposes
491 than cropland. Consequently, the area in Fig. 5b will be ranked higher than area in Fig. 5a when selecting which grid cells of
492 croplands will be removed from the map in order to match the total cropland area with historical statistical data.

493

494

495

496
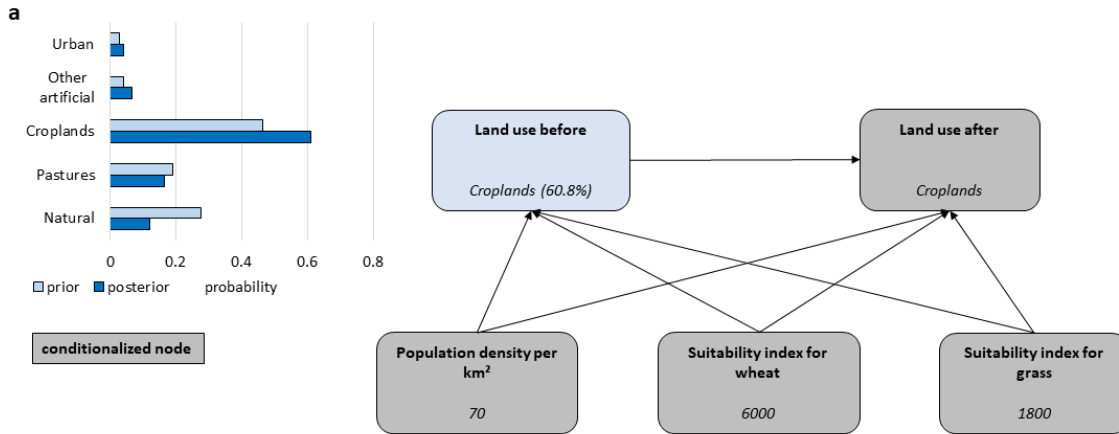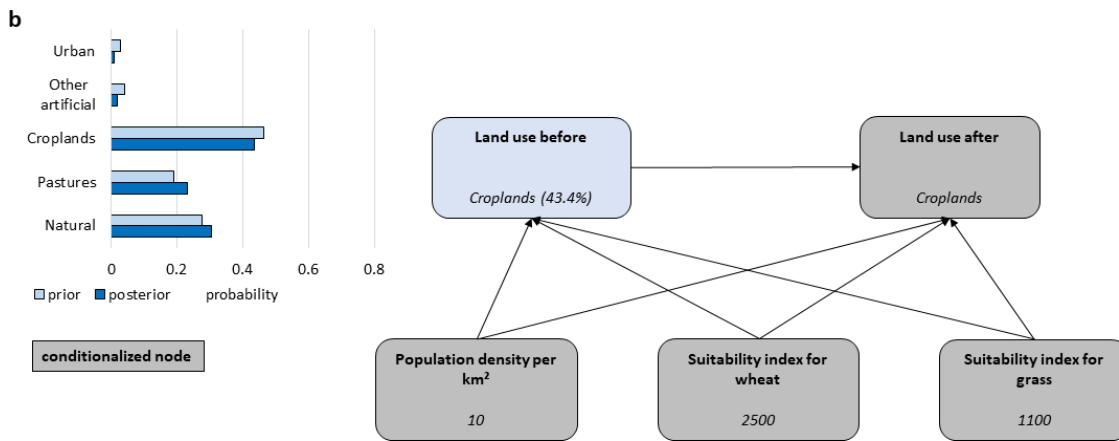
Figure 5. Example of a conditionalized Bayesian Network for land-use transitions. Panel (a) shows a highly-suitable area for croplands, and (b) an unsuitable one. The graph indicates the prior (situation in Fig. 4) and posterior (nodes in grey being conditionalized with values indicated) probability of previous land-use type (60.8% in (a) and 43.4% in (b) for being croplands).

501

The trained BN is used to generate probabilities of land-use transitions in nine cases, as follows:

- from non-urban to urban after the baseline year;
- from non-cropland to cropland after the baseline year;
- from non-pasture to pasture after the baseline year;
- from cropland to non-cropland after the baseline year;
- from pasture to non-pasture after the baseline year;

- from non-cropland to cropland before the baseline year;

- from non-pasture to pasture before the baseline year;

- from cropland to non-cropland before the baseline year;

- from pasture to non-pasture before the baseline year.

As noted in section 2.4.3, the BN handles the case of non-urban to urban transition after 2011. When the housing needs of the population result in expansion of cities, areas with the highest probability of transition from non-urban to urban land-use are build-up first. The BN is used in the same way for the remaining eight cases related to agriculture, i.e. they determine in which agricultural areas to add or remove so that the total area of croplands and pastures in the land cover map for a given time step matches the values obtained from historical statistics per NUTS3 region. This is done iteratively starting with patches of land with the highest probability of transition between given classes (e.g. non-pasture to pasture). Cropland redistribution is modelled first, then pasture is redistributed in the second step. Land still occupied by croplands after the first step cannot transition to pasture. However, land emptied by redistribution of croplands in the first step can transition to pasture in the second step.

We need to model transitions backward in time for timesteps before 2011. We partially remove urban fabric or roads/railways sites in case they occupied less land in the past and create an empty space, which croplands can occupy. Forward in time, it is a cropland to non-cropland transition. The probability of transition that is used to determine which cells to fill with croplands is the probability that a non-cropland cell was a cropland before. The same applies to pastures, with the condition that they cannot occupy cells already assigned to cropland. Transition of artificial surfaces still remaining at this step of the model to agricultural land-use is not allowed.

In the iterative land-use redistribution process, the number of grid cells with equal probability of transition might exceed the number of cells that need to be converted to match the total area in the historical statistics. This often happens as the predictors (GAEZ dataset and population density by VLAU) have relatively coarse resolution together with a small number of bins in which the data is divided. In order to derive exact 100-m grid cells from patches of land of equal probability, another predictor of agricultural suitability was added. Slope of the terrain is an important predictor, also used in the two agricultural suitability indices from FAO. It is available in the target (100 m) resolution as a continuous quantity from the EU-DEM elevation dataset (Eurostat 2022). Lower slope indicates better suitability for agricultural activity, therefore 100 m cells of equal probability of transition are ranked according to the slope from lowest to highest. The appropriate number of highest-ranked cells is added/removed so that the total area of croplands or pastures exactly matches the total area in the historical statistics.

2.4.11 Burnt areas

Areas where vegetation has burned down (typically forests) are by definition a temporary land use. Burnt areas are very short-lived: almost none of the land cover patches in this class (CLC 334) in 2012 were present in either 2006 or 2018 CLC inventories. For years 2007–2017, burnt area was assumed constant, while for years 1870–2006 and 2018–2020 all burnt areas

were removed from the dataset. As almost all burnt areas are formerly or subsequently CLC classes 311–324, this modelling step is done after redistributing agricultural areas. Still, there is no exposure in burnt areas, and very little exposure in preceding land-use, except for rare cases

2.4.12 Forest and other natural land

Natural areas are what remains after modelling artificial, agricultural and burnt areas as well as reservoirs and special cases. Natural areas would cover the entire continent without human activity. Therefore, if land becomes unoccupied as a result of the modelling, it is assigned the same natural land cover that is typical in its nearest neighbourhood. Typical natural vegetated land cover (classes CLC 311–324 and 411–422) is defined as the most frequently occurring one within the VLAU. The calculation is done separately for forests (CLC 311–313) and other natural land (CLC 321–324 and 411–422), and the more frequent of the two groups is used. If there is no natural cover in the VLAU, the dominant vegetated land cover of the applicable NUTS3 region is used. If no vegetated land cover was located in the NUTS3 region, the unoccupied land was assumed to be covered by transitional woodland-shrub (CLC 324), as it is the most common non-forest natural land in the study area.

After the first allocation, the total area of forests is compared with the historical data in the NUTS3 database. If there is too much forest area in a given NUTS3 region, the land that was allocated to forest in this step is iteratively converted into the most frequent non-forest class, starting with the most-densely populated VLAU. Conversely, if there is not enough forest land, cells that were allocated to non-forest vegetation in this step are iteratively converted into the most frequent forest class, starting with the least-densely populated VLAU.

All other natural land, without vegetation and usually prohibitive to construction or agriculture, i.e. beaches, dunes, sands (CLC 331), bare rocks (CLC 332), glaciers and perpetual snow (CLC 335), intertidal flats (CLC 423), and water (CLC 511-523), were kept constant throughout. Patches of this land use are removed from the map only in connection to reservoir or polder construction (see sections 2.4.1 and 2.4.4).

2.4.13 Soil sealing change map

Changes in soil sealing are entirely based on land-use transitions, therefore this step is carried out after land-use modelling, but before economic data disaggregation (section 2.5). Soil sealing in the baseline map is increased to the average value for a given CLC class (Table 6) when non-artificial land transitions to artificial, unless it is already higher than that value. For the backward in time calculation for timesteps before 2011, wherever land that is currently artificial is changed to agricultural, the degree of soil sealing is reduced alongside to 1%. Similarly, it is reduced to 0% in cases when agricultural or artificial land is changed to natural land.

Table 6. Average soil sealing in the Imperviousness 2012 dataset per selected types of Corine Land Cover classes.

CLC classes	Average soil sealing in 2012
Urban fabric (111–112)	28%
Industrial or commercial units (121)	45%
Road and rail networks (122)	29%
Airports (124)	20%
Agricultural areas (211–244)	1%
Natural land (311–523)	0%

2.5. Economic data disaggregation

The disaggregation of economic data follows dasymetric mapping methods, similar to applied in European (e.g. Batista e Silva et al. 2019) or global (e.g. Murakami and Yamagata 2019) studies, including HANZE v1.0. Several revisions to the latter were introduced. Soil sealing was added as a predictor next to population and land use, as indicated in Table 5. Regional GDP is split partially proportionally to population and partially according to land-use (with soil sealing where appropriate). In this way, both labour (part of the total population) and capital (connected to land-use) input to GDP is represented. Labour share of GDP in advanced countries is about 60% and has been relatively stable over time (ILO and OECD 2015). Hence, 60% of GDP is disaggregated according to population and the remaining 40% using land use. Fixed assets in absolute terms per region are computed by multiplying regional GDP, or a sector thereof, by the respective wealth-to-GDP ratio for each sector, as defined by variables "Fixed assets" listed in Table 2 (section 2.3). Housing and consumer durables are distributed according to total population, as they are most closely related to population distribution. Other assets, related to economic activities, are distributed to appropriate land use classes, proportionally to the degree of soil sealing. Finally, infrastructure is distributed to urban and industrial land (CLC classes 111–121) proportionally to the area covered by roads and streets, and to roads/railways, ports, and airports (CLC classes 122–124) proportionally to the degree of soil sealing.

There are also additional assumptions on disaggregation of GDP and wealth for two sectors. Agricultural sector encompasses farming, fishing and forestry, while the industrial sector includes mining, manufacturing, and utilities. A detailed breakdown of those subsectors is not available at regional level for GDP, or at all for fixed assets, except for a small number of countries. Hence the regional GDP and wealth from forestry and mining was estimated by computing "efficiency indices" at national level. The forestry index was compiled by computing GDP from agriculture (without forestry) at national level per ha of agricultural land from CLC and GDP from forestry per ha of forest land. Those values were computed for the year 2000 for

all countries and presented as efficiency of the forest economy relative to other agriculture in %. This ratio was used to compute the relative share of forestry in regional GDP in any given year based on land cover/use modelled for that year:

$$G_{f,r,t} = G_{af,r,t} \frac{A_{f,r,t} E_{f,c}}{(A_{a,r,t} + A_{f,r,t} E_{f,c})} \tag{16}$$

where G is GDP, A is area covered by land cover/use in a particular sector, E_c is the efficiency index for country c. The forest sector is denoted by f, agricultural sector (without forestry) by a, NUTS3 region by r and timestep by t. Agricultural GDP without forestry is therefore:

$$G_{a,r,t} = G_{af,r,t} - G_{f,r,t} \tag{17}$$

The wealth-to-GDP ratio for agriculture is used for both forestry and other agriculture. Mining and quarrying are split from the remaining industrial activities (manufacturing and utilities) using a mining efficiency index, calculated like the forest index. In the same way, it uses the proportion of mining areas (CLC 131) relative to industrial areas (CLC 121) in each NUTS3 region and timestep to disaggregate the two sectors. Equations 16 and 17 are applicable with substituting the different sectors and land-use types. The wealth-to-GDP ratio for industry is used for both mining and other industries.

Table 7. Disaggregation of economic variables by population and land use classes (CLC = Corine Land Cover class codes).

Variable	Category	Population	Land use	Soil sealing
GDP	Agriculture excl. forestry	Population in CLC 211–244 (60%)	CLC 211–244 (40%)	-
	Forestry	Population in CLC 311–313 (60%)	CLC 311–313 (40%)	-
	Industry excl. mining	Total population (60%)	CLC 121 (40%)	yes
	Mining	Total population (60%)	CLC 131 (40%)	-
	Services	Total population (60%)	CLC 111–124/133/141/142 (40%)	yes
Wealth	Housing	Total population	-	-
	Consumer durables	Total population	-	-
	Agriculture excl. forestry	-	CLC 211–244	yes
	Forestry	-	CLC 311–313	yes
	Industry excl. mining	-	CLC 121	yes
	Mining	-	CLC 131	yes
	Services	-	CLC 111–121/133/141/142	yes
	Infrastructure	-	CLC 111–124	yes (streets and roads for CLC 111–121)

2.6 Validation & comparison datasets

Validating high-resolution exposure data is a challenge due to limited availability of comparable observational datasets. Here, we utilise available population and land-use data for validation and further compare the results with other published modelled datasets. Validating the disaggregation of economic data is currently not possible due to the lack of data.

2.6.1 Population disaggregation

There is a general lack of very high-resolution population reference data (Leyk et al. 2019), partially due confidentiality reasons. The GEOSTAT 1 km grid is already modified in some countries (see metadata in the Excel input file "Region_database_population_lu") for that reason. It provides the highest resolution available for an observational product. Therefore, we prepared an alternative disaggregation of 1 km population to 100 m using floor space of residential buildings as predictor, rather than aggregated land-use and soil sealing data. High-resolution building vector data (GUGiK 2022) for municipalities in Poland threatened by sea level rise from Paprotny and Terefenko (2017) are used here. The data is accurate as of 2012/2013, which is close to the census date (2011). Within each 1 km grid cell completely within the validation area, we computed the residential floor space in m² using the area of residential buildings, multiplied by the number of stories, per 100 m grid cell of our high-resolution population grid. The population was distributed proportionally to floor space in each 100 m cell. For the calculation we excluded collective-living facilities in which people do not normally register addresses, summer houses or abandoned buildings.

We compare our modelled results with the alternative disaggregation and a previously-published 100 m disaggregation of GEOSTAT called GHS (Freire et al. 2016). We computed false negative and positive ratios for the study area for both HANZE v2.0 and GHS. Those grids were then intersected with pan-European flood hazard maps (riverine from Alfieri et al. 2014 and coastal from Paprotny et al. 2019). Median absolute error in total exposed population by municipality was computed for administrative units with at least 30 persons exposed in the reference data (48–53 units, depending on the maps). The results are discussed in section 3.2.1.

2.6.2 Population change

The most detailed level at which validation of the modelled population changes is possible is the municipality level. We obtained two reference datasets for this purpose. First, we use the pan-European dataset (1960–2010) with population data by local administrative unit that was applied in the statistical analysis in section 2.4.2 and is described in detail in the Supplementary Text S1. Secondly, we assembled a dataset with a longer timespan for Austria. Statistik Austria (2022) has published historical census data recomputed to present-day municipalities, hence it was possible to combine this data, interpolated where necessary, with municipal boundaries from the Bundesamt für Eich- und Vermessungswesen (2022). The resulting reference population dataset covers the entire time span of this study (1870–2020) and 2117 units (all municipalities plus the districts of Vienna), see Supplementary Fig. S8. For further comparison we use the HYDE 3.2 dataset (Klein

Goldewijk et al. 2017), recomputed from 5' resolution to municipalities. Both HANZE and HYDE utilise subnational population data that is disaggregated both in space and time, making them the closest comparable exposure products. The results are discussed in section 3.2.2.

2.6.3 Land cover/use change

Validation of land cover/use change is based on samples of CLC and CLC-Changes from 2000 to 2018. Those samples were drawn as described in section 2.4, but the number of samples per cell was capped at 15, resulting in 97,790 samples each for transitions and non-transitions. The net amount of land that transitioned is known from historical statistics, hence a defined number of cells with the highest probability of transitioning according to the Bayesian Network model is selected. A validation metric can therefore be the percent of top-ranked cells, up to the amount that is known to have transitioned between defined land-use classes, that was correctly identified by the model. As the number of cells in different land-use classes varies, the success rate has to be contrasted with a random result, i.e. the success rate of randomly picking land-use cells as transitioning. Overall land cover/use modelling results in HANZE are compared with HILDA (Fuchs et al. 2011, 2013, 2015). It has a resolution of 1 km, containing changes in land cover/use for six classes (aggregated from CLC classification) from 1900 to 2010 over a domain of 29 countries and territories (the European Union without Croatia, but with the United Kingdom, plus Switzerland and the Isle of Man). HILDA is primarily a model that reallocates land-use based on aggregate historical statistics and probability maps, similarly to HANZE and HYDE. However, it also integrates, where possible, digitised historical maps. On the other hand, HILDA is primarily focused on agricultural land and its interaction with natural vegetation, which is of less interest in this study due to relatively low exposure related to those land cover categories. The results are discussed in section 3.2.3.

2.6.4 Exposure per flood event

The model enables computing exposure within defined hazard zones that cover only parts of NUTS3 regions together with uncertainty bounds. For that purpose, we added pan-European hazard maps with a 100-year return period (riverine from Alfieri et al. 2014 and coastal from Paprotny et al. 2019) to the input data files. Then, we ran the model using the option to sample the copula model of subnational population redistribution and the Bayesian Network for land-use transitions, rather than using mean predictions. Running multiple simulations with random sampling enabled deriving uncertainty bounds of exposure within defined hazard zones. Then, exposure was summed over the hazard zones located within NUTS3 regions that were impacted by historical events (information taken from HANZE v1.0, Paprotny et al. 2018a), assuming independence of exposure trends in different regions. This enables "normalizing" the flood losses that have occurred in any given year to a single benchmark year under the assumption of unchanged level of hazard and vulnerability. It should be noted that the river flood maps used here indicate flood hazard only among relatively large rivers, namely those with catchment areas of at least 500 km². The results are discussed in section 3.2.4

3. Results

3.1 Overview

In the past 150 years covered by the model, exposure has grown significantly in the study area: population increased by more than 130%, the number of households jumped almost fivefold, GDP 29-fold in constant prices and fixed assets 31-fold. Urban population almost quadrupled whereas rural population declined by nearly 40% (see Supplementary Fig. S9). Coupled with massive expansion of transport infrastructure, this caused the area covered by artificial surfaces to triple. Spatially, the patterns differ greatly between locations. Fig. 6 shows the increase, and sometimes decrease, in the population exposed to river floods (using maps from Alfieri et al. 2014) in the past 150 years, aggregated to NUTS3 regions for visualisation (see Supplementary Fig. S10 for an equivalent figure for coastal floods). The native 100 m resolution is only visible when zooming into a smaller part of the dataset area. We present the example of Munich in Fig. 7. Population increase has driven the expansion of urban fabric, industry, and infrastructure, while economic growth has multiplied the value of fixed assets in the region.
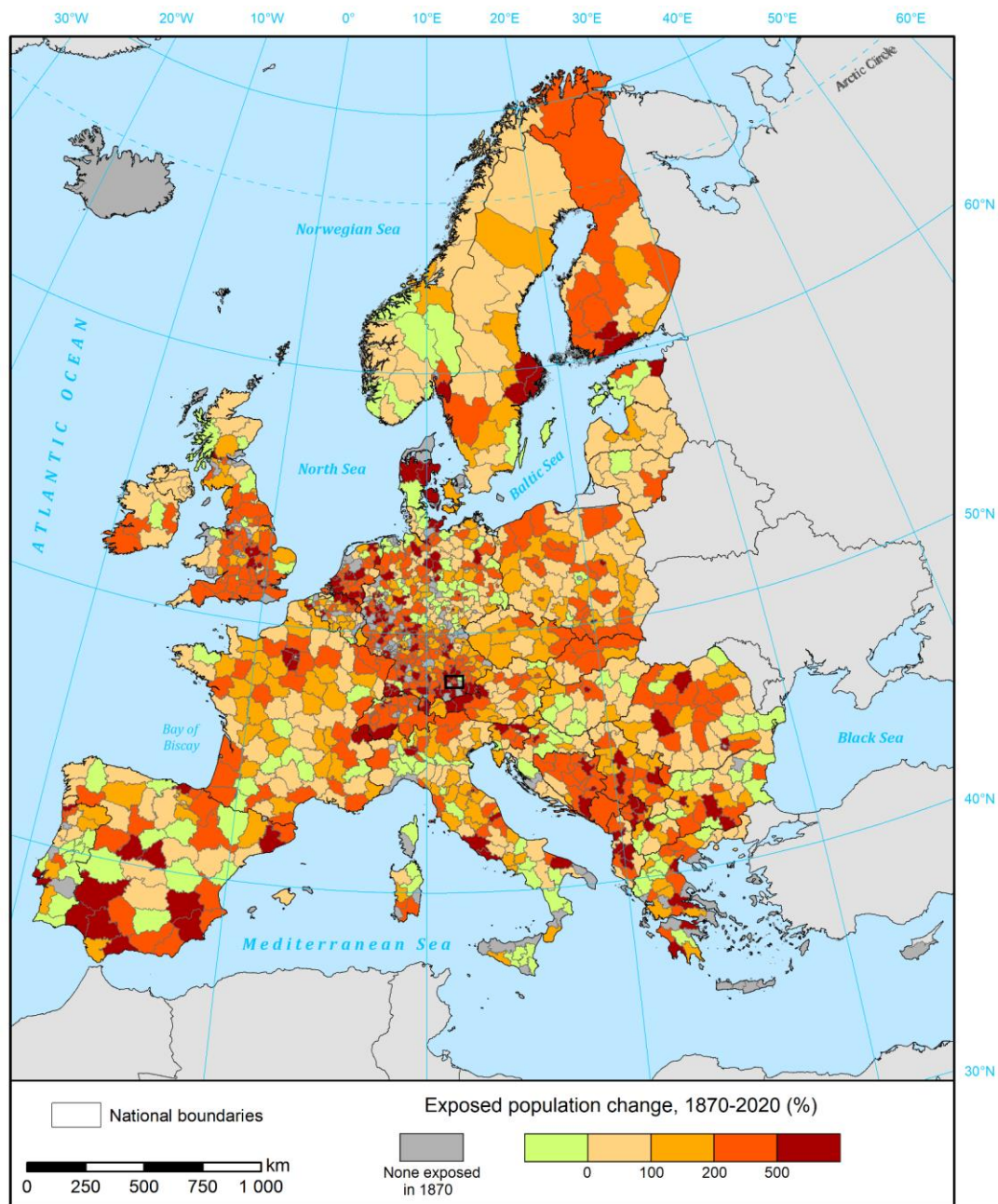
Figure 6. Change in the population number within 100-year river flood zones (from Alfieri et al. 2014, minimum catchment area 500 km²), 1870–2020, aggregated from 100 m resolution to NUTS3 regions. The black box indicates the Munich area shown in Fig. 6. National boundaries outside the study area based on Natural Earth (2022).
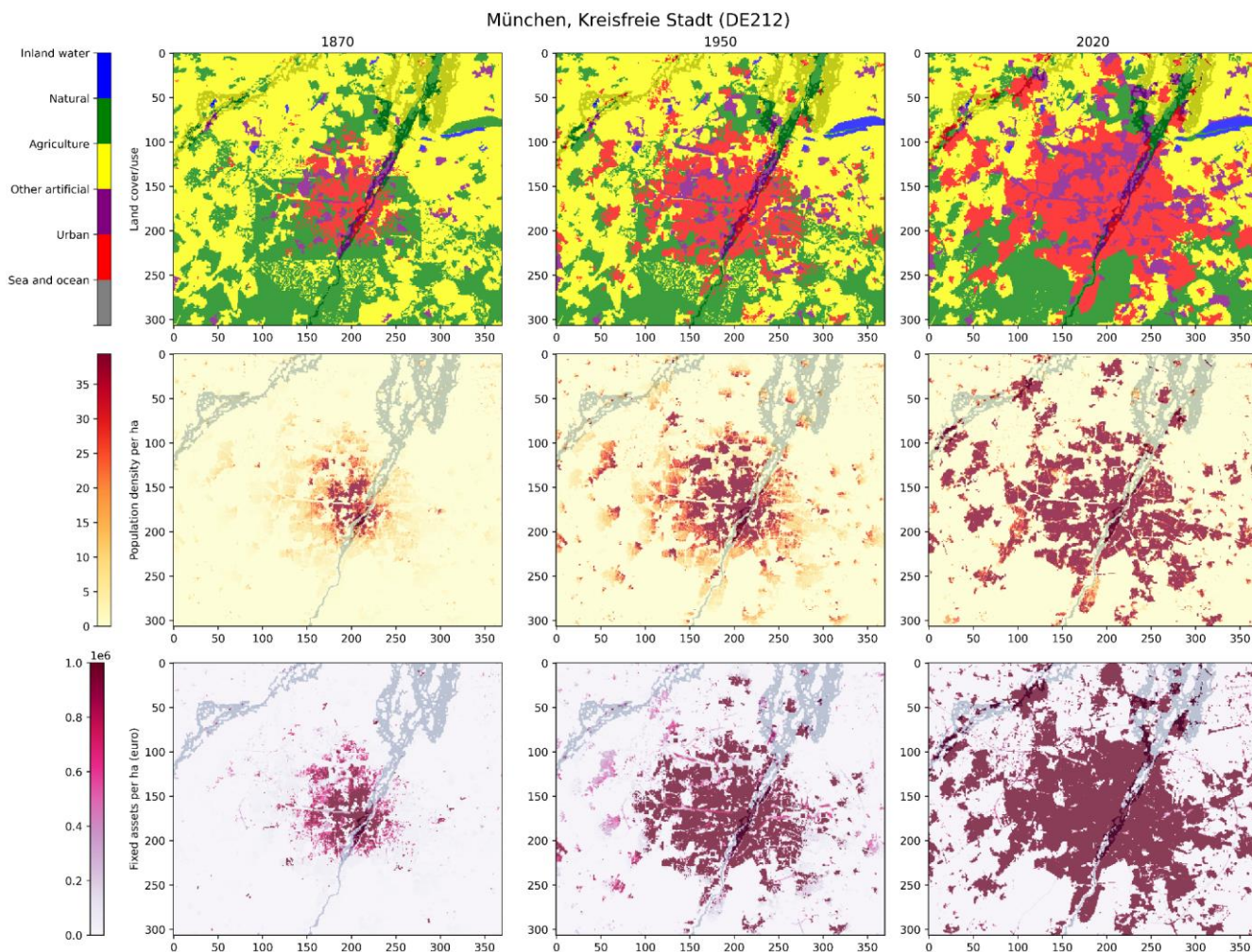
Figure 7. An example of modelled exposure growth in Munich, southern Germany, between 1870 and 2020, contrasted with a 100-year river flood map (grey shading). Figure generated with the model's code. Flood hazard zone from Alfieri et al. (2014).

Overall, exposure has grown faster within the European flood hazard zones than outside: population has grown within the river hazard zone by 193% [95% confidence interval: 168–216%] and the coastal hazard zone by 252% [228–268%], compared with increases of 131–132% in areas not endangered by floods. The same pattern was found for GDP and fixed assets, though less pronounced and additionally no increase or even decrease in the share of GDP/assets exposed to floods was found since the 1960s/1970s (Fig. 8).

695
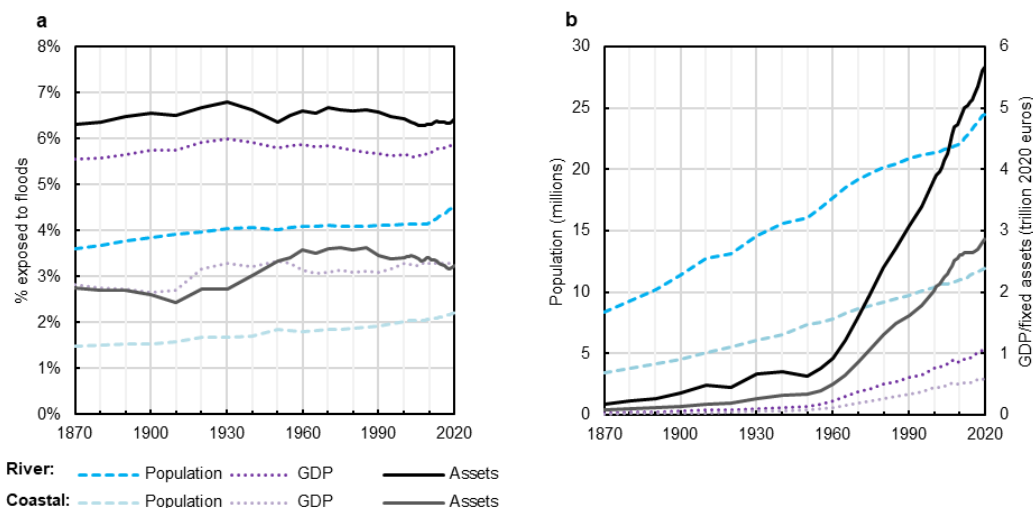
Figure 8. Exposure to river and coastal floods in Europe, 1870–2020 in relative (a) and absolute (b) terms. It is assumed that the extent of flood hazard zones doesn't change relative to the present climate. Flood hazard zones according to Alfieri et al. (2014) and Paprotny et al. (2019).

3.2 Validation

3.2.1 Population disaggregation

We compare HANZE, the Joint Research Centre's GHS population grid and the disaggregation based on building vector data (our benchmark dataset, see sec. 2.6.1). Both the HANZE and GHS grids smooth the spatial distribution of population too much, as indicated by false positive ratios (Table 6). Almost 40% of populated cells in HANZE have no population indicated in the benchmark dataset, though in half of those cases the indicated population is only one or two persons. The false positive ratio is higher in GHS than in HANZE and above 40%. Conversely, HANZE rarely indicates no population wrongly: only 3.5% of cells not populated in HANZE are populated in the benchmark dataset. This is less than the 4.7% in GHS (false negative ratio in Table 6). Exposure within river and coastal flood zones for municipalities of the Polish coastal zone was mostly represented well, with a median error of above 10% in HANZE. HANZE achieved better results than GHS for river flood hazard zones, though exposure to coastal flood was better modelled by GHS. A final check of the datasets was carried out by binning the population per 100 m grid cells in intervals of increasing by factor of 2: [0,1], [1,2], [2,4], [4,8], [8,16] etc. We found that the population per cell in HANZE was within +/- 1 interval of the validation dataset in 53% of the cases, which is better than 44% computed for the GHS dataset.

Table 8. Accuracy of population disaggregation to 100 m resolution in this study and in the GHS grid, compared with the benchmark dataset (alternative disaggregation using residential building vector data).

Metric	This study	GHS
False negative ratio	3.5%	4.7%
False positive ratio	37.5%	40.9%
Median absolute error in total exposed population by municipality for coastal floods	11.6%	8.3%
Median absolute error in total exposed population by municipality for river floods	10.3%	12.1%

3.2.2 Population change

Accuracy of population change at the level of local administrative units (LAUs) was analysed using the average absolute difference in modelled and observed population per LAU relative to observed population in a given year. Observed population was compiled from various sources as described in section 2.6.2. The metric is an average weighted by population size of LAU in a given year. As Fig. 9a indicates, error grows as more time elapses from the baseline year, reaching an average of about 20% by 1960 (in both validation areas) and 40% by 1870 (in Austria). However, the majority of LAUs are small rural communities, with more than half of LAUs in Europe having a population of less than 1000 in 1960, and a third in Austria in 1870 (Table 9). Both European and Austrian LAUs have changed population by more than a factor of two since 1960 and 1870, respectively. Therefore, absolute errors are mostly small (less than 200 persons in half of the LAUs in Europe). In larger LAUs, the relative errors are smaller (Table 7), though in Austria in 1870 errors in particular the districts of Vienna dominated the largest grouping of LAUs. The error varies by country (Fig. 9b) and is partially connected to the size of LAUs (relatively small in France or the United Kingdom, large in Poland and Greece) or the number of LAUs per NUTS3 region (on average 381 in France, but only 28 in Germany). Countries with large LAUs or small NUTS3 regions show less significant errors. In general, HANZE shows lower errors than HYDE, with small exceptions, for instance in Austria after 1980, though the population changes in that period were rather small compared to previous decades. From all major countries, France and Belgium show higher errors in HANZE than in HYDE in estimating population in 1960, while among small countries this only occurs for Luxembourg and Slovenia.
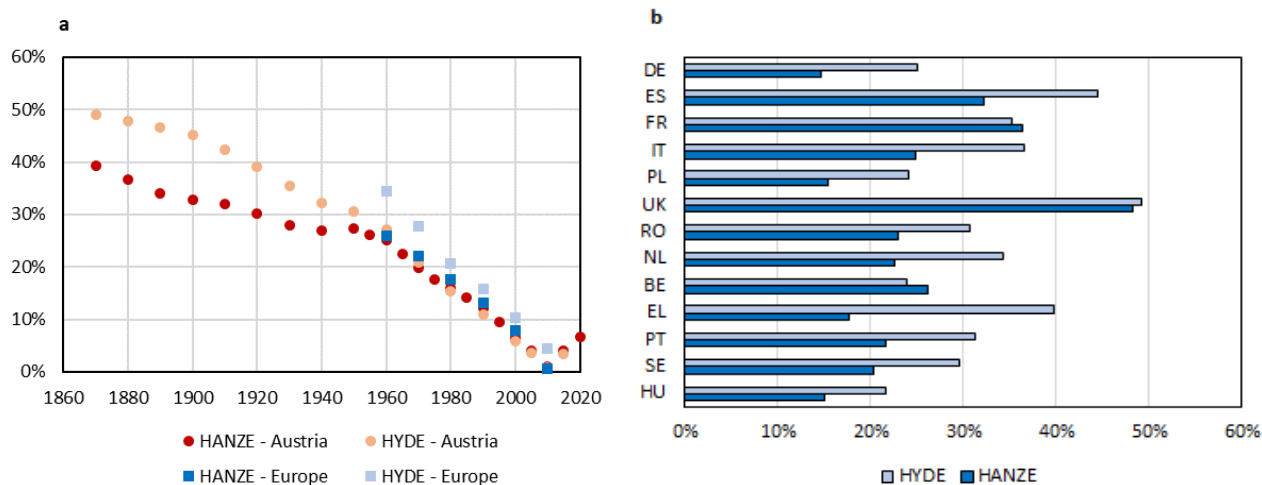
Figure 9. Accuracy of population change estimation compared with HYDE dataset. The error metric (in %) indicates average absolute difference in modelled and observed population per LAU relative to observed population in a given year. See section 2.6.2 for sources of observational data.

Table 9. Correctly identified transitions of land use in the validation dataset.

LAU population class	Number of LAUs (% share)	Population in LAUs (% share)	Average relative error (%) - HANZE	Average relative error (%) - HYDE
Europe, 1960				
<1000 persons	53%	6%	46%	58%
1000–9999 persons	40%	34%	32%	39%
10000 and more	7%	60%	20%	30%
Austria, 1870				
<1000 persons	36%	10%	54%	52%
1000–2499 persons	47%	35%	31%	36%
2500 and more	17%	55%	41%	57%

3.2.3 Land cover/use change

Validation results based on samples of CCL and CLC-Changes are presented in Table 10. In all considered cases of land-use transitions, the model's success rate in correctly identifying transitioning cells in the validation dataset is much higher than if cells were picked randomly.

Table 10. Correctly identified transitions of land use in the validation dataset.

Transition	Modelled	Random result
Other to urban	32%	7%
Other to cropland	51%	20%
Other to pasture	23%	5%
Cropland to other	62%	33%
Pasture to other	36%	13%

Comparison with HILDA indicates some important similarities with HANZE. The area of artificial surfaces has a very similar trend in the two datasets between 1900 and 1990 (Fig. 10a), even though HANZE was calibrated only for years 2000–2018. This indicates that the underlying processes do not strongly change over time and the model is also applicable to times before the calibration period. HILDA indicates almost no growth in artificial surface area after 1990, in contrast to HANZE. However, CLC and other datasets indicate strong growth. For instance, the LUCAS land-use survey data (Eurostat 2022) for 23 countries show that artificial surface expansion of 11% in only nine years (2009–2018). Cropland change is similar in both datasets (Fig. 10b) as largely similar data sources were used after 1950. Before that date HANZE used various national statistical data, while HILDA interpolated historical statistics or maps from 1950 backwards to 1900. The datasets differ significantly for pastures and forests. HILDA indicates a strong decrease in the area covered by pastures, which are replaced mostly by forests. By contrast, the historical statistics collected for HANZE do not indicate a decline in pasture area or growth in forest land as found in HILDA (see Supplement Fig. S9c). However, because there is no detailed model for transitions between forest land cover and other natural land in HANZE, reforestation of various natural land types that fall under "pastures" category in HILDA is not captured. Due to the low exposure and negligible importance for flood risk assessment of areas where these transitions occur we do not address them with a more detailed model. Finally, HILDA indicates a decline in area covered by water, which is opposite to HANZE, where reservoir construction leads to the overall expansion of water bodies in Europe.
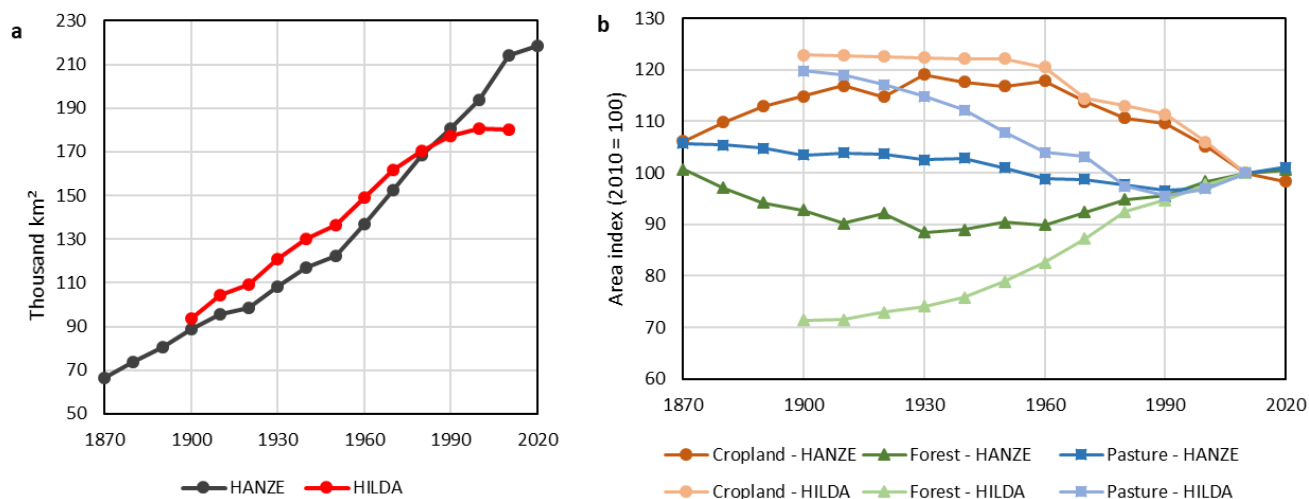
Figure 10. Artificial surfaces in thousand km² (a) and other main land use classes relative to year 2010 (b) in HANZE (this study) and HILDA, for the 29 countries and six aggregated CLC land cover/use classes available in HILDA (see 2.6.3).

3.2.4 Reported disaster losses and exposure change

Five illustrative event examples are shown in Fig. 11/12 and Table 11 to highlight how varied, and at times uncertain, exposure changes can be. The map in Fig. 11 presents population change within flood footprints of those events. Economic growth has been very strong everywhere in the study area. Smaller maps in Fig. 12 present exposure change between 1870 and 2020 in the Adige basin, one of the affected areas, with middle panels showing the timestep of HANZE closest to the year of the 1928 flood event. The other examples can be found in Supplementary Fig. S11.

The event in south-western France in March 1930 affected a large area in the Garonne, Agout and Tarn basins after several days of exceptional rainfall. Strong and continuous population growth was recorded in the region, almost threefold since the event. Assuming constant flood intensity and vulnerability, if the same event happened today, it would have been a 10-billion-euro disaster. Another event caused by heavy spring rainfall, in the Adige river basin (north-eastern Italy) in March-April 1928 does not seem very damaging if analysing only the nominal losses at that time, which amounted to 90 million euro (at 2020 price level). The population within the footprint of the event has grown by no more than a third since then, but assets in the area have grown much more strongly: when adjusting with fixed asset growth, more than 2 billion euro would have been lost today. Adjusting the loss with GDP leads to lower "normalized" loss of about 0.7 billion euro. This highlights the uncertainty when correcting the monetary estimate of losses. The differences stem from structural changes in the economy and evolution of wealth-to-GDP ratio for the different sectors, and changes in spatial distribution of population and assets. Still, historical estimates of flood losses almost exclusively pertain to direct loss of tangible assets, hence normalization by fixed assets is

786 more suitable. The ratio between losses normalized by fixed assets and losses normalized by GDP is a measure for the coping

787 capacity, as when asset replacement value grows faster than incomes, it becomes more difficult to afford the losses incurred.

788 A major flood in the Tisza river basin (eastern Hungary) in May-June 1970 happened, as our data show, at the peak of

789 population exposure in the area. After growing strongly in the late 19th and early 20th century, population stagnated in the

790 affected area and has declined by around 10% since the flood occurred. In the case of the catastrophic coastal flood in Hamburg

791 caused by the highest storm surge in two centuries in February 1962, the trend of growing population exposure is clear.

792 However, the large uncertainty especially in the first half of the 20th century is noticeable. At the same time, the median

793 estimate is close to the lower bound. This indicates that a significant portion of the flood hazard zone is located on the edges

794 of the city, where new development has taken place, but most likely still unbuilt until recent decades. The final example is a

795 coastal flood that affected the Estonian city of Pärnu in January 2005, the only major flood in that country recorded in HANZE

796 v1.0. Exposure changed rather little since this relatively recent event, but the past is more complicated with disruption caused

797 by World War II clearly visible. The abrupt reduction in population in an otherwise slowly increasing trend creates large

798 uncertainty on the exact distribution of population and, consequently, assets, in the preceding decades. After a period of quick

799 rebound, the population stagnated in recent decades. Similarly to Hamburg, hazard zones are largely on the edges of urban

800 areas, where it is most uncertain where exactly and how fast the local artificial environment has changed.

801

802
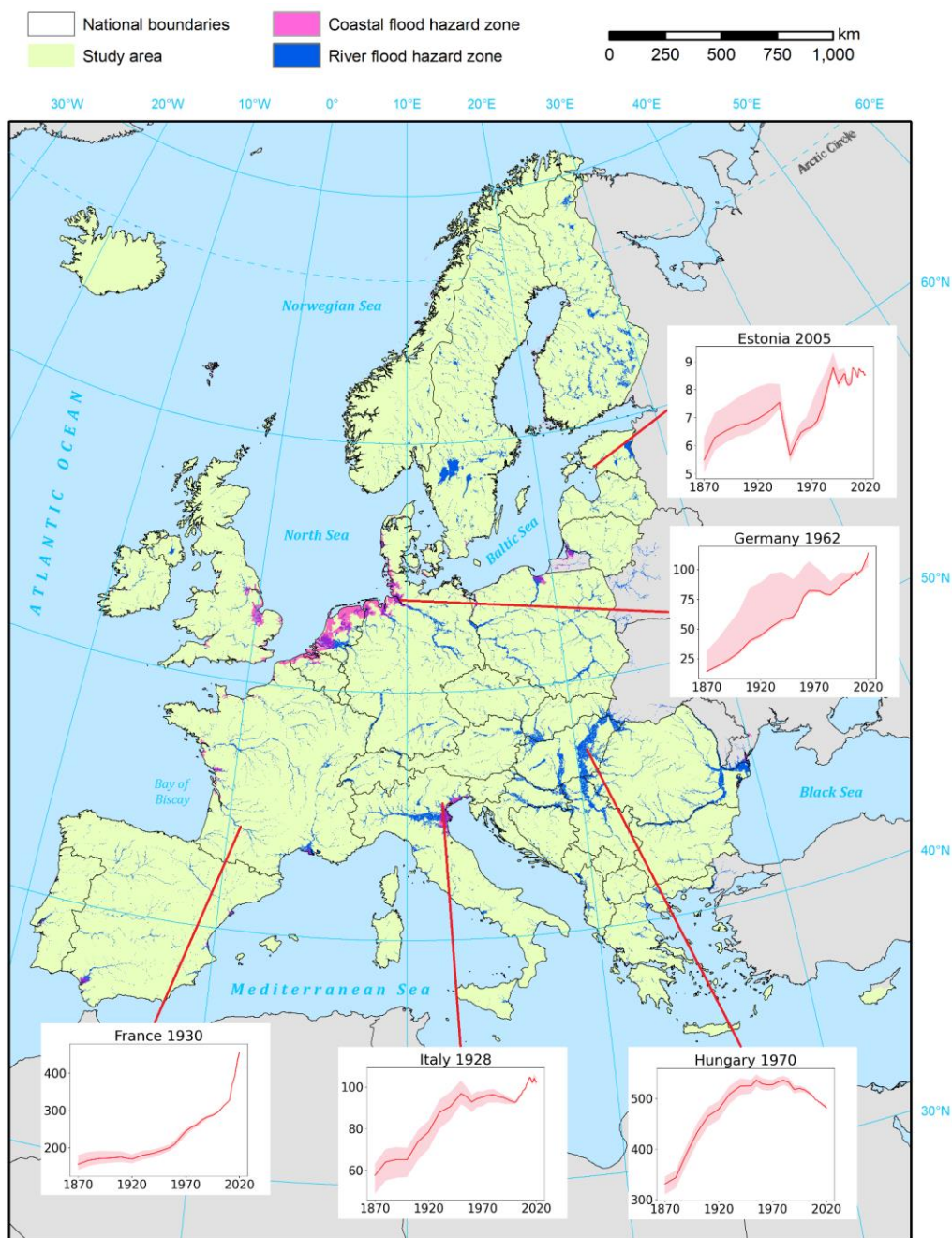
Figure 11. Flood hazard zones with a 100-year return period, not considering flood protection (coastal: Paprotny et al. 2019, riverine:
803
Alfieri et al. 2014). Graphs show median (red line) total population in thousands (1870–2020), with 95% uncertainty intervals (red
804
shadings) on the Y axis with years on the X axis, within the approximate footprints of large historical floods. Subplots were generated
805
using the model's code. National boundaries outside the study area based on Natural Earth (2022).
806

807

Table 11. Reported and normalized (exposure-adjusted) flood losses from large historical events (see also Fig. 5). Reported losses from HANZE v1.0. Normalized losses are shown with 95% uncertainty intervals. FA: fixed assets.

| Event | Reported losses at the time of the event | | | | Normalized losses at 2020 level of exposure | | | |
| | Fatalities | Persons affected ('000s) | Assets damaged (billions) | | Fatalities | Persons affected ('000s) | Assets damaged (billion euro) | |
			Original currency	2020 euros			GDP-adjusted	FA-adjusted
Coastal flood in Hamburg, Germany, 1962	315	20.0	2.5 [Mark]	5.8	454 [344–464]	28.8 [21.9–29.5]	16.2 [15.1–16.3]	28.7 [26.4–28.8]
Riverine flood in southern France, 1930	230	16.2	1.0 [Franc *germinal*]	0.8	582 [545–620]	41.0 [38.4–43.6]	10.4 [10.0–10.6]	7.8 [7.6–7.9]
Riverine flood in eastern Hungary, 1970	215	27.2	5.1 [Forint]	0.6	196 [193–200]	24.8 [24.4–25.4]	1.60 [1.58–1.62]	2.35 [2.33–2.37]
Riverine flood in north-eastern Italy, 1928	0	6.5	0.08 [Lira]	0.09	0	7.7 [7.2–8.5]	0.65 [0.64–0.67]	2.25 [2.19–2.34]
Coastal flood in Pärnu, Estonia, 2005	1	3.15	0.75 [Kroon]	0.09	1	3.29 [3.19–3.31]	0.09	0.10
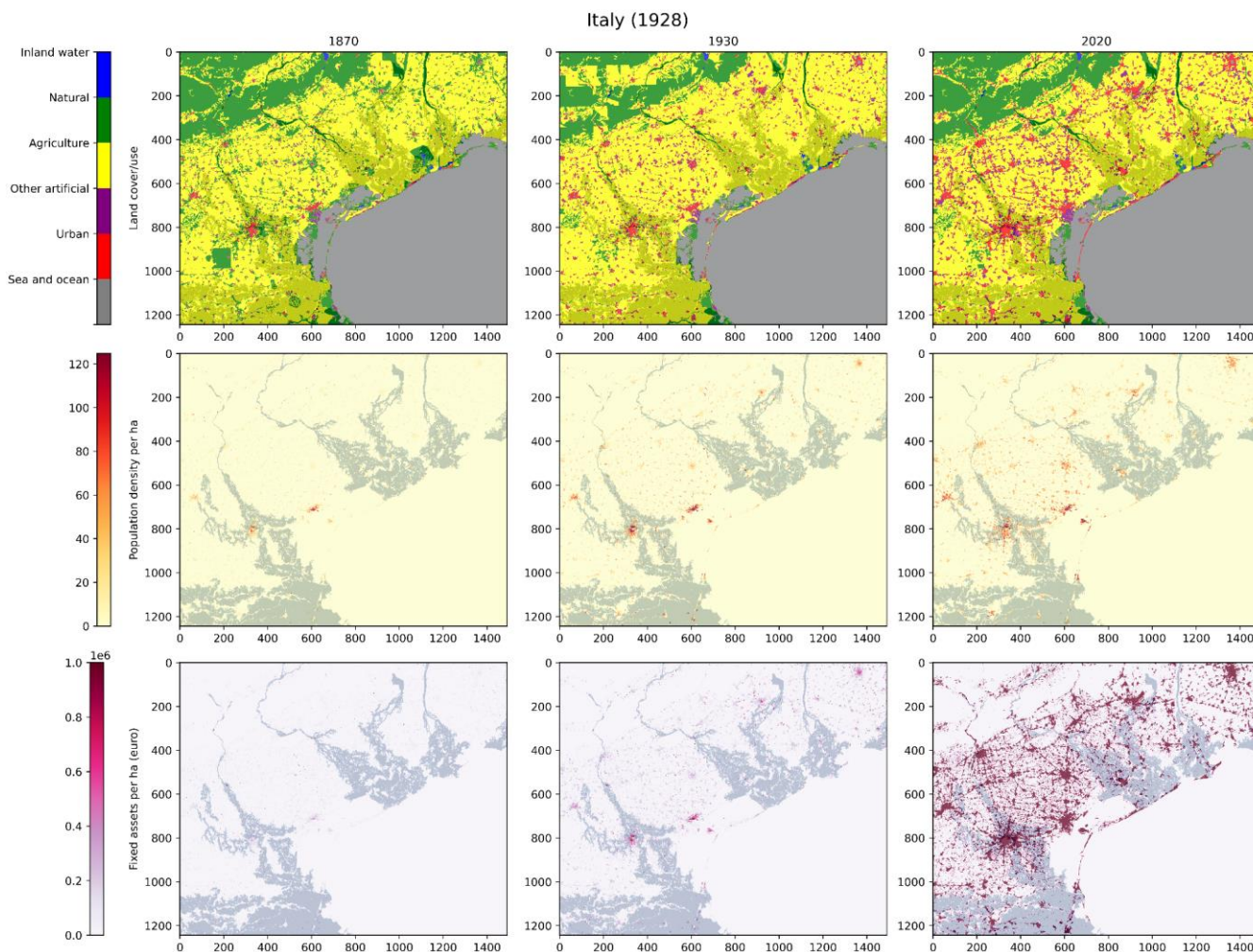
Figure 12. Land cover/use, population and fixed asset distribution around the area affected by the 1928 river flood in the Adige basin, in 1870, 1930 and 2020, contrasted with the 100-year river flood hazard zone (grey shading) from Paprotny et al. (2019). Figure generated with the model's code.

4. Usage

The user can apply the model's code in several ways. All input datasets (Supplementary Table S3) are available from the repository (see "Code and data availability"), hence the user only needs only to download them and change the defined path to the folder with data. Then, the code can be run using the basic options embedded in the code, which are:

- generating five exposure rasters (land cover/use, population, GDP, fixed assets, soil sealing) in GeoTIFF format and 100 m resolution. A single year or multiple years out of those included in the database (10-yearly 1870–1950, 5-yearly 1950–2000, annually 2000–2020) could be run. Also, all NUTS3 regions could be included, or only a single

821   NUTS3 region, or several regions. The output exposure maps are also available in the repository, as even if the model
822   is rather efficient given its resolution (about one hour for one timestep for all NUTS3 regions), computing all 40
823   timesteps of the study would require large resources or time.

824   ● computing exposure (population, GDP, fixed assets) per hazard zone. A raster file with the same spatial extent as the
825   other input raster files is needed for this. Example files are provided in the repository, which enable reproducing the
826   analysis presented in section 3.2. Using this option, a text file with data (for years defined by the user) is saved
827   separately for each NUTS3 region.

828   ● computing exposure with uncertainty bounds per hazard zone. This is an extension of the previous option, which
829   saves a text file per region and variable (population, GDP, fixed assets) with the 5th, 20th, 50th, 80th, and 95th percentile.

830   The code also enables, for reproducibility, computing some of the input data. Many of the input datasets required extensive
831   one-off preparations, hence only certain pre-processing steps could be included. Importantly, the population disaggregation
832   routine described in section 2.2.2 can be rerun. The population thresholds for dasymetric mapping can also be recomputed, as
833   well as the probability maps used in land-use modelling (section 2.4). Code for reproducing the validation of population change
834   (section 3.2.2) and land-use change (section 3.2.3) is also included. Finally, the code enables visualising selected exposure
835   information per flood event (from HANZE v1.0) in the form of graphs (like the subplots in Fig. 11) and maps (as in Fig. 12)
836   as well as reproducing Fig. 7 for any user-defined NUTS3 region.

837   The model can be used beyond the temporal or spatial setting defined in it, though this requires user-defined input data
838   (corresponding to those listed in Supplementary Table S3). Complexity of such adjustments depends on the desired outcomes:

839   ● To apply the model for different timesteps, the necessary historical statistics (i.e. all of those listed in Table 2) have
840   to be added to the input Excel files ("Region_database_population_lu" and "Region_database_economy"). In
841   principle, this possibility could be used to create exposure maps for future scenarios.

842   ● To run a different NUTS region definition, apart from adapting the historical statistics, the vector map with the
843   administrative boundaries and attributes would need replacing together with a corresponding raster file.

844   ● To run the model in a completely different domain, all input files (historical statistics, vector map of regions and all
845   rasters) need to be replaced with data that have a consistent definition of regional units and the same spatial extent.

846   **5. Discussion**

847   **5.1 Limitations**

848   The model is in principle applicable in another domain, or to create future projections (e.g. disaggregating the global Shared
849   Socio-Economic Pathways, or SSP, scenarios), but might not necessarily be the right model. This is because the processes that
850   are represented are those that were observed in Europe (without Eastern Europe) in the past 150 years. The subcomponents of
851   the model were quantified or calibrated based on high-resolution historical data specific for the continent in a particular time

frame. In some cases, calibration parameters could be easily changed in the model (weights for distance from urban centre, urban fabric transition or population disaggregation thresholds, elasticity of industrial area to production). In other crucial elements, such as the Bayesian Network for land-use transitions or the copulas for sub-regional populations, changes would require more substantial effort.

As noted in the introduction, the HANZE is not a general-purpose land-use change model. Its focus on high-exposure areas: urban, industrial and agricultural results in natural land cover being modelled only parsimoniously or not at all. Changes in natural areas are represented as a consequence of encroachment of artificial or agricultural land, additionally modelled mainly in the reverse chronological sequence. Consequently, transitions between e.g. forests and grasslands are not represented by a dedicated sub-model. Some elements of infrastructure (e.g. ports) are kept constant in the model due to the lack of necessary data in the temporal dimension. Still, this has a small impact on the exposure distribution, as only about 1% of both population and assets are located in natural areas or those covered by infrastructure excluded from modelling (Table 3). The change in population distribution and asset value per unit area is applied across all land cover and use types.

5.2 Uncertainties

Several elements of the model generate uncertainty on the distribution of exposure at any given time point. The lowest uncertainty is related to the baseline layers, as they are the most precise products currently available. The 1 km population grid is almost entirely based on enumerated and georeferenced population, while the disaggregation performed here has shown favourable results relative to an alternative high-resolution benchmark dataset. There is a tendency to smooth the population distribution, which is difficult to avoid without more precise building data. The land cover/use and imperviousness datasets have nominal thematic accuracy of >85% and >90%, respectively (Copernicus Land Monitoring Service 2022), but misclassifications could locally strongly affect the disaggregation of population and asset value.

Historical statistics that drive the model come from a vast array of heterogeneous sources. Whereas data on total population is generally taken from accurate census records and available in high spatial detail, the availability of other regional data and their comparability between countries vary to a larger degree. Official statistics on GDP and fixed assets have mostly short time series, and economic data beyond the recent decades are predominantly scientific reconstructions of varying detail and accuracy. Historical land cover/use and urban population data are affected by large differences in classification between countries and time periods. For all variables, inaccuracies could be introduced when recomputing data produced for historical administrative divisions to NUTS version 2010 (or data from newer NUTS editions, for that matter). Actual availability of NUTS3 data for population (total/urban) and GDP is summarised in Supplementary Fig. S2.

Disaggregation of economic data has considerable uncertainty, mainly regarding GDP. In contrast to fixed assets, which have a defined geographical location, GDP can be allocated to different places, depending on the approach to measure it. Three main approaches exist: the production, income and the expenditure approach. Even at NUTS3 level, GDP is often problematic to measure (European Union 2013). Here, we apply the income approach, splitting GDP into labour (disaggregated according

884 to population) and capital (disaggregated by land-use) inputs. Using the production approach would have allocated a majority

885 share to land-use, making the distribution very similar to fixed assets. The expenditure approach is not feasible already at

886 NUTS3 level (European Union 2013). The labour/capital shares were simplified here to 60/40, even though the exact value

887 varies by country and year. Data over longer time periods are not available for most countries, hence the simplification of a

888 fixed 60/40 ratio.

889 Finally, the most significant source of uncertainty are the model components. It is a combination of statistical and rule-based

890 methods, focused on high-exposure areas, developed knowing the major constraint of data availability. Validation data is also

891 limited and indicates that the model's performance varies by country and drops the further it diverges from the baseline year.

892 For the elements of the model using probabilistic methods (sub-regional population, agricultural land-use) the uncertainty is

893 quantified and can be calculated for any user-defined hazard zone. Comparison with other datasets (GHS population grid,

894 HILDA historical land use dataset) indicate that HANZE achieves similar or better results despite simplifying inputs and

895 methods. Improved resolution of historical statistics results in better reconstruction of past population distribution than the

896 global HYDE dataset that uses an approach similar to HANZE (in essence, disaggregating land-use and population changes

897 defined in historical data).

6. Conclusions

899 HANZE is an openly-accessible model and dataset intended to support natural hazard research in Europe. The main application

900 of the model is deriving exposure (demographic and economic) for any defined hazard zone or disaster footprint at any point

901 in time since 1870. Past trends in events impacts on the population or the economy can't be properly understood or attributed

902 to changing climate without considering how exposure changed in the temporal dimension. Availability of hazard maps and

903 footprints of historical events is not constrained to floods (Dottori et al. 2022), but covers e.g. wildfires (Giglio et al. 2018)

904 and windstorms (Copernicus Climate Change Service 2022). Examples presented in section 3.2 highlight how different local

905 exposure trends can be within Europe.

906 Yet, the model could support climate change attribution in other aspects. Land cover/use and soil sealing maps could inform

907 changes in impervious and agricultural land, which affect river runoff and therefore magnitude of flood hazard, especially in

908 small river basins (Sebastian et al. 2019). Land cover/use, population and GDP all influence water use, another important

909 factor in hydrological modelling (Vandecasteele et al. 2014). Therefore, HANZE could be a basis for creating factual and

910 counterfactual scenarios for European hydrological models (Alfieri et al. 2016) that consider human influence on the

911 environment beyond climate change. Vulnerability modelling, based on historical impact data, would be enabled by HANZE

912 not only by providing information on exposure at the time when a particular disaster occurred, but also providing predictors

913 of vulnerability. Paprotny et al. (2018b) has shown that vulnerability computed for major historical floods is correlated with

914 GDP per capita, population density, land use structure and wealth structure. In microscale, flood adaptation is correlated e.g.

915 with household income (Bubeck et al. 2012), which is a major component of GDP.

916 In the future, we expect to use the model for the array of applications highlighted above, with the ultimate goal of attributing

917 historical flood impacts to both environmental and economic drivers. This will involve collecting improved historical flood

918 impact data, the hydrodynamic modelling of historical floods and combining impact data with exposure computed in this work.

919

920 *Code and data availability*. The source code of HANZE v2.0 presented in the paper is archived at

921 https://dx.doi.org/10.5281/zenodo.6826536. The input data are archived at https://dx.doi.org/10.5281/zenodo.6783023. The

922 output maps and results of uncertainty estimation from section 3.2 are archived at https://dx.doi.org/10.5281/zenodo.6783202.

923 Flood impact data (used in section 3.2.4), with a description of sources of the data, are available in the HANZE v1.0 repository,

924 https://dx.doi.org/10.4121/collection:HANZE. Data for validation of population estimates for Europe (section 3.2.2) are

925 largely based on information published through Eurostat (see Supplementary Text S3) and have to be obtained from the authors

926 on request.

927 *Supplement*. A supplemental document with additional text, figures and tables referred in the text is available to this paper.

928 *Author contributions*. DP developed the concept, implemented the methods, wrote the code, produced the data and acquired

929 funding. MM supervised the work. All authors wrote the paper.

930 *Competing interests*. The authors declare that they have no conflict of interest.

931 *Acknowledgements*. We thank Diego Rybski, Yunfei Li and Manon Glockmann for technical discussions on the model's

932 methodology.

933 *Financial support*. This research has been supported by the German Research Foundation (DFG) through project

934 "Decomposition of flood losses by environmental and economic drivers" (FloodDrivers), grant no. 449175973.

935 **References**

936 Alfieri, L., Salamon, P., Bianchi, A., Neal, J., Bates, P., and Feyen, L.: Advances in pan-European flood hazard mapping,
937   Hydrol. Process., 28, 4067–4077, doi:10.1002/hyp.9947, 2014.

938 Alfieri, L., Feyen, L., Salamon, P., Thielen, J., Bianchi, A., Dottori, F., and Burek, P.: Modelling the socio-economic impact
939   of river floods in Europe, Nat. Hazards Earth Syst. Sci., 16, 1401–1411, doi:10.5194/nhess-16-1401-2016, 2016.

940 Almar, R., Ranasinghe, R., Bergsma, E.W.J., Diaz, H., Melet, A., Papa, F., Vosudoukas, M., Athanasiou, P., Dada, O.,
941   Almeida, L. P., and Kestenare, E.: A global analysis of extreme coastal water levels with implications for potential coastal
942   overtopping, Nat. Commun., 12, 3775, doi:10.1038/s41467-021-24008-9, 2021.

943 Antonescu, B., Schultz, D. M., Holzer, A., and Groenemeijer, P.: Tornadoes in Europe: An underestimated threat, Bull. Am.
944   Meteorol. Soc., 98, 713–728, doi:10.1175/BAMS-D-16-0171.1, 2017.

945 Barendrecht, M. H., Viglione, A., Kreibich, H., Merz, B., Vorogushyn, S., and Blöschl, G.: The value of empirical data for
946   estimating the parameters of a sociohydrological flood risk model, Water Resources Research, 55, 1312–1336,
947   doi:10.1029/2018WR024128, 2019.

948 Barredo, J. I.: Normalised flood losses in Europe: 1970–2006. Nat. Hazards Earth Syst. Sci., 9, 97–104, doi: 10.5194/nhess-9-
949   97-2009, 2009.

950 Barredo, J. I.: No upward trend in normalised windstorm losses in Europe: 1970–2008, Nat. Hazards Earth Syst. Sci., 10, 97–
951   104, doi:10.5194/nhess-10-97-2010, 2010.

952 Batista e Silva, F., Gallego, J., and Lavalle, C.: A high-resolution population grid map for Europe, J. Maps, 9(1), 16–28,
953   doi:10.1080/17445647.2013.764830, 2013.

954 Batista e Silva, F., Forzieri, G., Marin Herrera, M. A., Bianchi, A., Lavalle, C., and Feyen, L.: HARCI-EU, a harmonized
955   gridded dataset of critical infrastructures in Europe for large-scale risk assessments, Sci. Data, 6, 126,
956   doi:10.1038/s41597-019-0135-1, 2019.

957 Bubeck, P., Botzen, W. J. W., and Aerts J. C. J. H.: A Review of Risk Perceptions and Other Factors that Influence Flood
958   Mitigation Behavior, Risk Anal., 32, 1481-1495, doi:10.1111/j.1539-6924.2011.01783.x, 2012.

959 Bundesamt für Eich- und Vermessungswesen: Verwaltungsgrenzen (VGD) - Stichtagsdaten grundstücksgenau,
960   https://www.data.gv.at/katalog/dataset/verwaltungsgrenzen-vgd-stichtagsdaten-grundstucksgenau, 2022, last accessed
961   15 February 2022.

962 Carisi, F., Schröter, K., Domeneghetti, A., Kreibich, H., and Castellarin, A.: Development and assessment of uni- and
963   multivariable flood loss models for Emilia-Romagna (Italy), Nat. Hazards Earth Syst. Sci., 18, 2057–2079,
964   doi:10.5194/nhess-18-2057-2018, 2018.

965 Clark, C. (1951) Urban Population Densities. Journal of the Royal Statistical Society: Series A, 114(4), 490–496, 1951.

966 Copernicus Land Monitoring Service: Pan-European, http://land.copernicus.eu/pan-european/, last accessed 6 May 2022.

967 Copernicus Climate Change Service: Winter windstorm indicators for Europe from 1979 to 2021 derived from reanalysis,
968   Climate Data Store, doi:10.24381/cds.9b4ea013, last accessed 6 May 2022.

969 Dawkins, L. C., Stephenson, D. B., Lockwood, J. F., and Maisey, P. E.: The 21st century decline in damaging European
970   windstorms, Nat. Hazards Earth Syst. Sci., 16, 1999–2007, doi:10.5194/nhess-16-1999-2016, 2016.

971 Dawkins, L. C. and Stephenson, D. B.: Quantification of extremal dependence in spatial natural hazard footprints:
972   independence of windstorm gust speeds and its impact on aggregate losses, Nat. Hazards Earth Syst. Sci., 18, 2933–2949,
973   doi:10.5194/nhess-18-2933-2018, 2018.

974 Dottori, F., Alfieri, L., Bianchi, A., Skoien, J., and Salamon, P.: A new dataset of river flood hazard maps for Europe and the
975   Mediterranean Basin, Earth Syst. Sci. Data, 14, 1549–1569, doi:10.5194/essd-14-1549-2022, 2022.

976 Eberenz, S., Stocker, D., Röösli, T., and Bresch, D. N.: Asset exposure data for global physical risk assessment. Earth System
977   Science Data, 12, 817–833, doi:10.5194/essd-12-817-2020, 2020.

978 European Union: European System of Accounts ESA 2010, Publications Office of the European Union, Luxembourg,
979   doi:10.2785/16644, 2013.

980 Eurostat: https://ec.europa.eu/eurostat, last accessed 15 February 2022.

FAO (2022) Global Agro-Ecological Zoning version 4 (GAEZ v4), https://gaez-data-portal-hqfao.hub.arcgis.com/, Last accessed 20 April 2022.

Formetta, G., and Feyen, L.: Empirical evidence of declining global vulnerability to climate-related hazards, Global Environmental Change, 57, 101920, doi10.1016/j.gloenvcha.2019.05.004, 2019.

Freire, S., Halkia, M., and Pesaresi, M.: GHS population grid, derived from EUROSTAT census data (2011) and ESM R2016, European Commission, Joint Research Centre (JRC) [Dataset] PID: http://data.europa.eu/89h/jrc-ghsl-ghs_pop_eurostat_europe_r2016a, 2016, last accessed 15 February 2022.

Frieler, K., Lange, S., Piontek, F., Reyer, C. P. O., Schewe, J., Warszawski, L., Zhao, F., Chini, L., Denvil, S., Emanuel, K., Geiger, T., Halladay, K., Hurtt, G., Mengel, M., Murakami, D., Ostberg, S., Popp, A., Riva, R., Stevanovic, M., Suzuki, T., Volkholz, J., Burke, E., Ciais, P., Ebi, K., Eddy, T. D., Elliott, J., Galbraith, E., Gosling, S. N., Hattermann, F., Hickler, T., Hinkel, J., Hof, C., Huber, V., Jägermeyr, J., Krysanova, V., Marcé, R., Müller Schmied, H., Mouratiadou, I., Pierson, D., Tittensor, D. P., Vautard, R., van Vliet, M., Biber, M. F., Betts, R. A., Bodirsky, B. L., Deryng, D., Frolking, S., Jones, C. D., Lotze, H. K., Lotze-Campen, H., Sahajpal, R., Thonicke, K., Tian, H., and Yamagata, Y.: Assessing the impacts of 1.5 °C global warming – simulation protocol of the Inter-Sectoral Impact Model Intercomparison Project (ISIMIP2b), Geosci. Model Dev., 10, 4321–4345, doi:10.5194/gmd-10-4321-2017, 2017.

Fuchs, R., Herold, M., Verburg, P.H., and Clevers, J.G.P.W.: A high-resolution and harmonized model approach for reconstructing and analysing historic land changes in Europe, Biogeosciences, 10(3), 1543–1559, doi:10.5194/bg-10-1543-2013, 2013.

Fuchs, R., Herold, M., Verburg, P.H., Clevers, J.G.P.W., and Eberle, J.: Gross changes in reconstructions of historic land cover/use for Europe between 1900-2010, Glob. Change Biol., 21(1), 299–313, doi:10.1111/gcb.12714, 2014.

Fuchs, R., Verburg, P. H., Clevers, J.G.P.W., and Herold, M.: The potential of old maps and encyclopaedias for reconstructing historic continental land cover/use change, Appl. Geogr., 59, 43-55, doi:10.1016/j.apgeog.2015.02.013, 2015.

Ganteaume, A., Camia, A., Jappiot, M., San-Miguel-Ayanz, J., Long-Fournel, M., and Lampin, C.: A review of the main driving factors of forest fire ignition over Europe, Environ. Manage., 51, 651-662, doi:10.1007/s00267-012-9961-z, 2013.

Geiger, T.: Continuous national gross domestic product (GDP) time series for 195 countries: past observations (1850–2005) harmonized with future projections according to the Shared Socio-economic Pathways (2006–2100), Earth Syst. Sci. Data, 10, 847–856, doi:10.5194/essd-10-847-2018, 2018.

Genest, C., Rémillard, B., Beaudoin, D.: Goodness-of-fit tests for copulas: A review and a power study, Insur. Math. Econ., 44, 199–213, doi:10.1016/j.insmatheco.2007.10.005, 2009.dotto

Giglio, L., Boschetti, L., Roy, D. P., Humber, M. L., and Justice, C. O.: The Collection 6 MODIS burned area mapping algorithm and product, Remote Sens. Environ., 217, 72-85, doi:10.1016/j.rse.2018.08.005, 2018.

Global Dam Watch: Global Reservoir and Dam Database (GRanD), http://globaldamwatch.org/grand/, last accessed 7 July 2021.

Grant, L., Vanderkelen, I., Gudmundsson, L., Tan, Z., Perroud, M., Stepanenko, V. M., Debolskiy, A. V., Droppers, B., Janssen, A. B. G., Woolway, R. I., Choulga, M., Balsamo, G., Kirillin, G., Schewe, J., Zhao, F., Vega del Valle, I., Golub, M., Pierson, D., Marcé, R., Seneviratne, S. I., and Thiery, W.: Attribution of global lake systems change to anthropogenic forcing. Nat. Geosci. 14, 849–854, doi:10.1038/s41561-021-00833-x, 2021.

Gudmundsson, L., Boulange, J., Do, H.X., Gosling, S.N., Grillakis, M.G., Koutroulis, A.G., Leonard, M., Liu, J., Müller Schmied, H., Papadimitriou, L., and Pokhrel, Y.: Globally observed trends in mean and extreme river flow attributed to climate change, Science, 371, 1159-1162, doi:10.1126/science.aba3996, 2021.

GUGiK: Zintegrowane kopie baz danych obiektów topograficznych BDOT10k, http://www.gugik.gov.pl/pzgik/zamow-dane/baza-danych-obiektow-topograficznych-bdot-10k, last accessed 24 June 2022.

Harrigan, S., Zsoter, E., Alfieri, L., Prudhomme, C., Salamon, P., Wetterhall, F., Barnard, C., Cloke, H., and Pappenberger, F.: GloFAS-ERA5 operational global river discharge reanalysis 1979–present, Earth Syst. Sci. Data, 12, 2043–2060, doi:10.5194/essd-12-2043-2020, 2020.

Huizinga, J., de Moel, H., and Szewczyk, W.: Global flood depth-damage functions. Methodology and the database with guidelines, report EUR 28552 EN, Publications Office of the European Union, Luxembourg, doi:10.2760/16510, 2017.

ILO and OECD: The Labour Share in G20 Economies. Report prepared for the G20 Employment Working Group, available at https://www.oecd.org/g20/topics/employment-and-social-policy/The-Labour-Share-in-G20-Economies.pdf, 2015.

IPCC: Climate Change 2021: The Physical Science Basis. Contribution of Working Group I to the Sixth Assessment Report of the Intergovernmental Panel on Climate Change, Cambridge University Press, 2021.

IPCC: Climate Change 2022: Impacts, Adaptation, and Vulnerability. Contribution of Working Group II to the Sixth Assessment Report of the Intergovernmental Panel on Climate Change, Cambridge University Press, 2022.

Jongman, B., Kreibich, H., Apel, H., Barredo, J. I., Bates, P. D., Feyen, L., Gericke, A., Neal, J., Aerts, J. C. J. H., and Ward, P. J.: Comparative flood damage model assessment: towards a European approach, Nat. Hazards Earth Syst. Sci., 12, 3733–3752, doi:10.5194/nhess-12-3733-2012, 2012.

Klein Goldewijk, K., Beusen, A., de Vos, M., and van Drecht, G.: The HYDE 3.1 spatially explicit database of human induced land use change over the past 12,000 years. Global Ecol. Biogeogr., 20(1), 73–86, doi:10.1111/j.1466-8238.2010.00587.x, 2011.

Klein Goldewijk, K., Beusen, A., Doelman, J., and Stehfest, E.: Anthropogenic land use estimates for the Holocene – HYDE 3.2, Earth Syst. Sci. Data, 9, 927–953, doi:10.5194/essd-9-927-2017, 2017.

Kreibich, H., Bubeck, P., Van Vliet, M. *et al.*: A review of damage-reducing measures to manage fluvial flood risks in a changing climate, Mitig. Adapt. Strateg. Glob. Change **20,** 967–989, doi:10.1007/s11027-014-9629-5, 2015.

Kummu, M., Taka, M., and Guillaume, J. H. A.: Gridded global datasets for Gross Domestic Product and Human Development Index over 1990–2015, Sci. Data, 5, 180004, doi:10.1038/sdata.2018.4, 2018.

Leyk, S., Gaughan, A. E., Adamo, S. B., de Sherbinin, A., Balk, D., Freire, S., Rose, A., Stevens, F. R., Blankespoor, B., Frye, C., Comenetz, J., Sorichetta, A., MacManus, K., Pistolesi, L., Levy, M., Tatem, A. J., and Pesaresi, M.: The spatial allocation of population: a review of large-scale gridded population data products and their fitness for use, Earth Syst. Sci. Data, 11, 1385–1409, doi:10.5194/essd-11-1385-2019, 2019.

McAneney, J., Sandercock, B., Crompton, R., Mortlock, T., Musulin, R., Pielke Jr., R., and Gissing, A.: Normalised Insurance Losses from Australian Natural Disasters: 1966-2017, Environ. Hazards, 18(5), 414–433, doi:10.1080/17477891.2019.1609406, 2019.

Mengel, M., Treu, S., Lange, S., and Frieler, K.: ATTRICI v1.1 – counterfactual climate for impact attribution, Geosci. Model Dev., 14, 5269–5284, doi:10.5194/gmd-14-5269-2021, 2021.

Metin, A. D., Dung, N. V., Schröter, K., Guse, B., Apel, H., Kreibich, H., Vorogushyn, S., and Merz, B.: How do changes along the risk chain affect flood risk?, Nat. Hazards Earth Syst. Sci., 18, 3089–3108, doi:10.5194/nhess-18-3089-2018, 2018.

Murakami, D. and Yamagata, Y.: Estimation of Gridded Population and GDP Scenarios with Spatially Explicit Statistical Downscaling, Sustainability, 11, 2106, doi:10.3390/su11072106, 2019.

Natural Earth: 1:10m Cultural Vectors, https://www.naturalearthdata.com/downloads/10m-cultural-vectors/, last accessed 8 September 2022.

O'Neill, B., M. van Aalst, Z. Zaiton Ibrahim, L. Berrang Ford, S. Bhadwal, H. Buhaug, D. Diaz, K. Frieler, M. Garschagen, A. Magnan, G. Midgley, A. Mirzabaev, A. Thomas, and R. Warren: Key Risks Across Sectors and Regions, in: IPCC, Climate Change 2022: Impacts, Adaptation, and Vulnerability. Contribution of Working Group II to the Sixth Assessment Report of the Intergovernmental Panel on Climate Change, Cambridge University Press, 2022.

OurAirports, Open data downloads, http://ourairports.com/data/, last accessed 6 July 2021.

Papagiannaki, K., Petrucci, O., Diakakis, M., Kotroni, V., Aceto, L., Bianchi, C., Brázdil, R., Gelabert, M. G., Inbar, M., Kahraman, A., Kılıç, Ö., Krahn, A., Kreibich, H., Llasat, M. C., Llasat-Botija, M., Macdonald, N., de Brito, M. M., Mercuri, M., Pereira, S., Řehoř, J., Geli, J. R., Salvati, P., Vinet, F., Zêzere, J. L.: Developing a large-scale dataset of flood fatalities for territories in the Euro-Mediterranean region, FFEM-DB, Sci. Data 9, 166, doi:10.1038/s41597-022-01273-x, 2022.

Paprotny D., and Terefenko P.: New estimates of potential impacts of sea level rise and coastal floods in Poland, Nat. Hazards, 85(2), 1249–1277, doi:10.1007/s11069-016-2619-z, 2017.

Paprotny D., Kreibich H., Morales Nápoles O., Wagenaar D., Castellarin A., Carisi F., Bertin X., Merz B., and Schröter K.: A probabilistic approach to estimating residential losses from different flood types, Nat. Hazards, 105(3), 2569–2601, doi:10.1007/s11069-020-04413-x, 2021.

Paprotny, D., Kreibich, H., Morales-Nápoles, O., Terefenko, P., and Schröter, K.: Estimating exposure of residential assets to natural hazards in Europe using open data, Nat. Hazards Earth Syst. Sci., 20, 323–343, doi:10.5194/nhess-20-323-2020, 2020.

Paprotny, D., Morales Nápoles, O., Vousdoukas, M. I., Jonkman, S. N., and Nikulin, G.: Accuracy of pan-European coastal flood mapping, J. Flood Risk Manag., 12(2), e12459, doi:10.1111/jfr3.12459, 2019.

Paprotny, D., Morales-Nápoles, O., and Jonkman, S. N.: Efficient pan-European river flood hazard modelling through a combination of statistical and physical models, Nat. Hazards Earth Syst. Sci., 17, 1267–1283, doi:10.5194/nhess-17-1267-2017, 2017.

Paprotny, D., Morales-Nápoles, O., and Jonkman, S. N.: HANZE: a pan-European database of exposure to natural hazards and damaging historical floods since 1870, Earth Syst. Sci. Data, 10, 565–581, doi:10.5194/essd-10-565-2018, 2018a.

Paprotny, D., Sebastian, A., Morales Nápoles, O., and Jonkman, S. N.: Trends in flood losses in Europe over the past 150 years, Nat. Commun., 9, 1985, doi:10.1038/s41467-018-04253-1, 2018b.

Paprotny, D.: Residential exposure to natural hazards in Europe, 2000–2020 [data set], 10.5281/zenodo.6573503, 2022.

Pielke, R.: Economic 'normalisation' of disaster losses 1998–2020: a literature review and assessment, Environ. Hazards, 20(2), 93-111, doi:10.1080/17477891.2020.1800440, 2021.

Sauer, I., Reese, R., Otto, C., Geiger, T., Willner, S., Guillod, B. P., Bresch, D. N., and Frieler, K.: Climate signals in river flood damages emerge under sound regional disaggregation. Nat. Commun., 12, 2128, doi:10.1038/s41467-021-22153-9, 2021.

Scussolini, P., Aerts, J. C. J. H., Jongman, B., Bouwer, L. M., Winsemius, H. C., de Moel, H., and Ward, P. J.: FLOPROS: an evolving global database of flood protection standards, Nat. Hazards Earth Syst. Sci., 16, 1049–1061, doi:10.5194/nhess-16-1049-2016, 2016.

Sebastian, A., Gori, A., Blessing, R. B., van der Wiel, K., and Bass B.: Disentangling the impacts of human and environmental change on catchment response during Hurricane Harvey, Environ. Res. Lett., 14, 124023, doi:10.1088/1748-9326/ab5234, 2019.

Simmons K. M., Sutter, D., Pielke, R.: Normalized tornado damage in the United States: 1950–2011, Environ. Hazards, 12(2), 132-147, doi:10.1080/17477891.2012.738642, 2013.

Statistik Austria: http://www.statistik.at/, last accessed 15 February 2022.

Steinhausen, M., Paprotny, D., Dottori, F., Sairam, N., Mentaschi, L., Alfieri, L., Lüdtke, S., Kreibich, H., and Schröter K.: Drivers of future fluvial flood risk change for residential buildings in Europe. Global Environ. Chang., 76, 102559, doi:10.1016/j.gloenvcha.2022.102559, 2022.

Stucki, P., Brönnimann, S., Martius, O., Welker, C., Imhof, M., von Wattenwyl, N., and Philipp, N.: A catalog of high-impact windstorms in Switzerland since 1859, Nat. Hazards Earth Syst. Sci., 14, 2867–2882, doi:10.5194/nhess-14-2867-2014, 2014.

United Nations: World Urbanization Prospects: The 2018 Revision, https://population.un.org/wup/, last accessed 21 June 2022.

Vandecasteele, I., Bianchi, A., Batista e Silva, F., Lavalle, C., and Batelaan, O.: Mapping current and future European public water withdrawals and consumption, Hydrol. Earth Syst. Sci., 18, 407–416, doi:10.5194/hess-18-407-2014, 2014.

Vousdoukas, M. I., Bouziotas, D., Giardino, A., Bouwer, L. M., Mentaschi, L., Voukouvalas, E., and Feyen, L.: Understanding epistemic uncertainty in large-scale coastal flood risk assessment for present and future climates, Nat. Hazards Earth Syst. Sci., 18, 2127–2142, doi:10.5194/nhess-18-2127-2018, 2018.

Vousdoukas, M. I., Voukouvalas, E., Mentaschi, L., Dottori, F., Giardino, A., Bouziotas, D., Bianchi, A., Salamon, P., and Feyen, L.: Developments in large-scale coastal flood hazard mapping, Nat. Hazards Earth Syst. Sci., 16, 1841–1853, doi:10.5194/nhess-16-1841-2016, 2016.

Welker, C., Röösli, T., and Bresch, D. N.: Comparing an insurer's perspective on building damages with modelled damages from pan-European winter windstorm event sets: a case study from Zurich, Switzerland, Nat. Hazards Earth Syst. Sci., 21, 279–299, doi:10.5194/nhess-21-279-2021, 2021.

Zanardo, S., Nicotina, L., Hilberts, A. G. J., and Jewson, S. P.: Modulation of economic losses from European floods by the North Atlantic Oscillation, Geophys. Res. Lett., 46, 2563–2572, doi:10.1029/2019GL081956, 2019.